catalysts

MDPI

Review

Photocatalysis for Air Treatment Processes: Current Technologies and Future Applications for the Removal of Organic Pollutants and Viruses

Salvador Escobedo and Hugo de Lasa *

Faculty of Engineering, Western University, Chemical Reactor Engineering Centre (CREC), 1151 Richmond Street, London ON N6A 5B9, Canada; sescobe@uwo.ca

* Correspondence: hdelasa@uwo.ca; Tel.: +1-519-661-2144; Fax: +1-519-850-2931

Received: 16 July 2020; Accepted: 21 August 2020; Published: 24 August 2020

Abstract: Photocatalysis for air treatment or photocatalytic oxidation (PCO) is a relatively new technology which requires titanium dioxide (TiO_2) and a source of light (Visible or near-UV) to degrade pollutants contained in air streams. Present approaches for the photodegradation of indoor pollutants in air streams aim to eliminate volatile organic compounds (VOCs) and viruses, which are both toxic and harmful to human health. Photocatalysis for air treatment is an inexpensive and innovative green process. Additionally, it is a technology with a reduced environmental footprint when compared to other conventional air treatments which demand significant energy, require the disposal of used materials, and release CO_2 and other greenhouse gases to the environment. This review discusses the most current and relevant information on photocatalysis for air treatment. This article also provides a critical review of (1) the most commonly used TiO_2-based semiconductors, (2) the experimental syntheses and the various photocatalytic organic species degradation conversions, (3) the developed kinetics and computational fluid dynamics (CFD) and (4) the proposed Quantum Yields (QYs) and Photocatalytic Thermodynamic Efficiency Factors (PTEFs). Furthermore, this article contains important information on significant factors affecting the photocatalytic degradation of organic pollutants, such as reactor designs and type of photoreactor irradiation. Overall, this review describes state-of-the-art photocatalysis for air treatment to eliminate harmful indoor organic molecules, reviewing as well the potential applications for the inactivation of SARS-CoV2 (COVID-19) viruses.

Keywords: Photocatalytic Oxidation (PCO); VOCs; TiO_2 based materials; light irradiation; kinetic modeling; CFD; QYs; PTEFs and COVID-19

1. Introduction

The generation of indoor air pollution by biological and chemicals contaminants including viruses, particles, polycyclic aromatic hydrocarbons (PAHs), combustion products and volatile organic compounds (VOCs) is a public health and environmental concern [1–3]. These agents may increase the risk of developing nonspecific respiratory and neurologic symptoms, allergies, asthma and lung cancer [4]. Since we spend a significant amount of time (on average 90%) in enclosed spaces such as homes, factories, office buildings and transportation vehicles, it is important to continuously remove VOCs and viruses from indoor air atmospheres [5,6]. Thus, by implementing new green technologies such as photocatalysis for air treatment, one may be able to achieve VOC removal and virus inactivation. Moreover, this new green process could lead to major policy mandated regulations for indoor building environments, as well as the establishment of a well-founded risk analysis [7].

Photocatalysis is an efficient technique that uses light photons and semiconductor materials under ambient reaction conditions in order to achieve the complete degradation of organic pollutants [8].

Among the different types of semiconductors, titanium dioxide (TiO_2) is by far one of the superior ones, given its high stability and photosensitivity, its high oxidation ability, its negligible toxicity and its low cost [9].

Photocatalytic reaction mechanisms for air treatment involve (a) light absorption, (b) the formation and separation of electron (e^-) and hole (h^+) pairs, and (c) oxidation-reduction surface reactions, occurring between electrons (e^-) and adsorbed oxygen molecules (O_2), which can produce superoxide radicals (O_2^-). Subsequently, additional electron holes (h^+) and water (H_2O) molecules can generate hydroxyl radicals ($OH^\bullet$). Thus, given that both O_2^- and $OH^\bullet$ radicals are powerful oxidants, they can mineralize harmful chemical species (i.e., VOCs) in air, converting them into CO_2 and H_2O, as later described in Figure 1 [2,10–15].

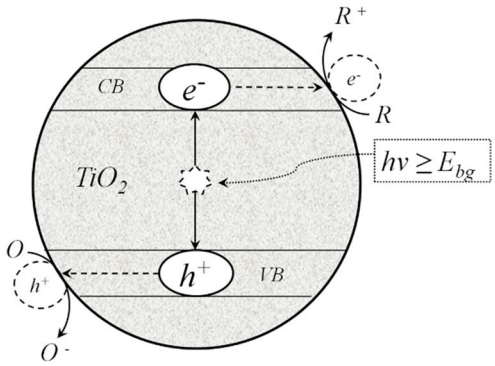

(**a**)

Light OFF

$$Organic\ Pollutant_{(g)} \xrightarrow{TiO_2} Organic\ Pollutant_{(ads)}$$
$$O_{2(g)} \xrightarrow{TiO_2} O_{2(ads)}$$
$$2H_2O_{(v)} \xrightarrow{TiO_2} 2H^+_{(ads)} + 2OH^-_{(ads)}$$

Light ON

$$TiO_2 \xrightarrow{hv} e^- + h^+$$
$$2OH^-_{(ads)} + h^+ \xrightarrow{TiO_2} 2OH^\bullet_{(ads)}$$
$$2H^+_{(ads)} + e^- \xrightarrow{TiO_2} 2H^\bullet_{(ads)}$$
$$O_{2(ads)} + e^- \xrightarrow{TiO_2} O^{\bullet-}_{2(ads)}$$
$$O^{\bullet-}_{2(ads)} + 2H^\bullet_{(ads)} \xrightarrow{TiO_2} 2OH^\bullet_{(ads)}$$

Photocatalytic Oxidation

$$Organic\ Pollutant_{(g)} + O_{2(g)} + 2H_2O_{(v)} \xrightarrow{TiO_2+3hv} 4OH^\bullet_{(ads)}$$
$$Organic\ Pollutant_{(ads)} + 4OH^\bullet_{(ads)} \xrightarrow{TiO_2} CO_{2(g)} + 2H_2O_{(v)}$$

(**b**)

Figure 1. General photocatalytic reaction mechanisms: (**a**) illustration of TiO_2 and energy photons interacting with adsorbed pollutants and (**b**) photochemical reaction steps.

Although TiO_2 semiconductors are promising, there are limitations preventing these photocatalysts from reaching their full potential. For example, TiO_2 displays high (e^-) and (h^+) charge recombination rates and a large energy band gap (E_{BG}) of 3.2 eV with only a small fraction of the solar spectrum being able to be used in photocatalytic applications. In addition, the popular commercial DP25 photocatalyst displays a small specific surface area with individual particle agglomeration as a result of the strong interparticle forces [16]. However, by impregnating, doping, or co-doping TiO_2 with metals such as iron (Fe), silver (Ag), palladium (Pd) and platinum (Pt) or non-metals like nitrogen (N), one can improve (a) the reduction of the TiO_2 energy band gap ($E_{BG} < 3.2$ eV), (b) the slowing of the (e^-)/(h^+) recombination rate, and (c) the diminishing of the particle agglomeration [17,18]. Furthermore, through the use of a new photocatalyst synthesis utilizing a sol-gel method, larger TiO_2 surface areas ($50\ m^2/g < S_{BET} \leq 150\ m^2/g$), morphologies (high porosity) and crystal structures (anatase dominant crystalline phase) can be obtained [11,19]. All these advancements with TiO_2 photocatalysts are extremely important for the improvement of the process of photocatalysis and the extensive application of air treatment, both for VOCs conversion and airborne virus inactivation.

During the past few years, numerous photoreactor configurations for PCO (Photocatalytic Oxidation) have been reported in the literature, including fixed-bed reactors [20–22], fluidized-bed reactors [23,24], coated honeycomb monolith reactors [25–27], fixed powder layer reactors [28,29],

annular coated reactors [11,30], and annular mesh-coated Venturi-reactors [2,12,13]. These reactor configurations are relevant given that they determine the PCO process. Their performance is affected by photocatalyst loading, the contacting between the fluid and the photocatalysts, as well as the uniformity, the type (near-UV or visible light) and the intensity of the irradiation field employed [9,14,31,32].

Nowadays, there is an increased need for PCO models based on chemical engineering principles. In this respect, a significant body of the research has focused on developing kinetic models in a variety of photocatalytic reactor configurations [8,31,33,34]. However, of similar importance is the study of computational fluid dynamics (CFD). The implementation of CFD has become possible thanks to the availability of powerful computers and the advancement of commercial CFD software. This allows numerical simulations for different reactor configurations and conditions relevant to industrial-scale applications [9,35–37]. It can be anticipated that CFD will help to design, develop, and analyze novel photocatalytic reactors (bench or pilot-scale) for air [2,12,14,38] or water treatment applications [39–41] and water splitting for hydrogen production [18,19,42].

This review also considers important photoreactor efficiency parameters such as Quantum Yields (QYs) and Photocatalytic Thermodynamic Efficiency Factors (PTEFs). A Quantum Yield describes the photoconversion of the organic pollutant in terms of the hydroxyl radicals consumed over the absorbed photons [10]. Furthermore, this efficiency factor has also been studied for water degradation [43] and hydrogen production [18,44]. To accurately evaluate this parameter, one has to measure macroscopic irradiation energy balances (MIEB) [15]. This strategy of assessing QYs and PTEFs allows the photocatalytic reactor to be operated under optimal conditions [8,15,16,43–45].

Thus, the present review is intended to report the most up-to-date research on air treatment for the removal of VOCs. Special emphasis has been given to new challenges, such as the inactivation of airborne viruses [46–49]. This review highlights research findings, research needs, and recent opportunities for innovation and commercialization of photocatalytic technologies for the inactivation of SARS-CoV2 (COVID-19) viruses.

2. Photocatalysts for Air Treatment

Commercial titanium dioxides (TiO_2) such as Degussa P25 or Hombikat UV-100 have already been studied during the last five decades. These photocatalysts are commonly used for purification of water [50] and of indoor air [51]. However, the development of new methods to synthesize TiO_2 for the photodegradation of organic pollutants is still an ongoing research activity. These approaches have focused on improving photocatalyst surface area, crystal structure, morphology and energy band gap (E_{BG}) [52]. In order to achieve this, for instance, some techniques such as doping and/or impregnation (dry or wet) allow one to incorporate non-metals (N, C or S) or metals (Mn, Co, Fe, V or Cr) into the TiO_2 lattice. One can also sensitize the TiO_2 surface with noble metals (Au, Ag, Pd or Pt) in order to enhance both its photocatalytic activity and energy band gap.

Table 1 reports a comparison of the most important properties of several reviewed commercial and non-commercial photocatalysts, doped and co-doped with different precursors.

Table 1. Comparison of different commercial and synthesized TiO_2-based photocatalysts for PCO.

Reference	Year	TiO_2-Based Photocatalysts	Crystalline Phase	Crystallite Size-$_{DB}$ (nm)	S_{BET} (m^2/g)	$V_{p\text{-}BJH}$ (cm^3/g)	$D_{p\text{-}BJH}$ (nm)	E_{BG} (eV)
[44]	2019	Evonik-Degussa P25 (DP25)	80% A 20% R	21	54	0.1	7.5	3.2
[10,53,54]	2001 2005 2016	Hombikat UV-100	99% A 1% R	<10	>250	-	≈10	3.2
[55]	2014	Cristal PC105	100% A	23	80	0.35	15	3.19
		Cristal AT-1		12	192	-	120	3.15
		Kronos Titan 1077			130	-	-	
[56,57]	2019	PC 500	100% A	9.5	345	-	-	3.35
		S5-300A		7.9	330	-	-	-
[58]	2011	1% Pt/N-TiO_2	-	5	94.5	-	6	2.69
[59]	2012	1.5% Fe-doped TiO_2	-	≈18	41.6	0.062	4	≈2.95
		≈1% S-doped TiO_2		≈14	42.7	0.186	≈15	≈3.18
		1.5% Fe/ ≈ 1% S co-doped TiO_2		≈1	77.8	0.191	7.7	≈3.01
[11]	2020	TiO_2	100% A	61.48	11.64	0.02	7.99	3.2
		5% N-TiO_2		11.45	122.80	0.19	5.87	3.02
		10% Ag-TiO_2		15.81	23.6	0.16	26.54	1.7
		5% N/Ag-TiO_2		11.47	81.16	0.26	15.97	1.5
[60]	2015	6 wt.% V-TiO_2/PU	-	-	192.5	-	-	2.83
[61]	2012	TiO_2	100% A	21.6	81.6	0.2	5.8	3.11
		S-TiO_2 (4)		15.6	51.7	0.13	4.8	2.7
		V_2O_5/TiO_2		35.2	66.3	0.15	4.6	2.8
		V_2O_5/S-TiO_2 (4)		32.7	16.5	-	-	2.5
[62]	2020	5 wt.% Co/TiO_2	100% A	≈11.1	≈80.4	-	6.1	≈2.76
[63]	2015	1 wt.% Mn/TiO_2	97% A 3% R	24.5	49.7	-	-	

Note: Acronyms are provided in Table Footnote as well as in the Nomenclature Section. Note: DB = Debye Sherrer Method; S_{BET} = Brunauer-Emmett-Teller Surface Area; BJH = Barrett-Joyner-Halenda Model; V_p = Pore Volume; D_p = Pore Diameter, E_{BG} = Energy Band Gap, A = Anatase and R = Rutile; and (x = 4) = S/Ti Molar Ratio.

2.1. Commercial TiO_2-Based Photocatalysts

TiO_2 is the most common and widely known semiconductor material employed for photocatalysis. Figure 1a,b describe the general reaction mechanism during the photocatalytic conversion of organic pollutants in air using a TiO_2 photocatalyst: a TiO_2 particle absorbs a photon with an energy content larger than or equal to 388 nm (3.2 eV). This event generates a pair of electrons (e^-) and electron holes (h^+) on the semiconductor surface, with electrons moving from the valence band (VB) to the conduction band (CB). These positively charged-electron pairs later react with the adsorbed organic species, which are simultaneously reduced ($R \rightarrow R^+$) and oxidized ($O \rightarrow O^-$) [64–68].

Ibrahim and de Lasa (2002) studied the effects of different loadings of two commercial photocatalysts designated as Degussa P25 and Hombikat UV-100 for acetone (C_3H_6O) photo-oxidation. Garcia-Hernandez et al. (2010) also used the aforementioned non-porous commercial photocatalysts for acetone and acetaldehyde (C_2H_4O) photodegradation in a Photo-CREC-Air as shown in Figures 5a,b and 6. These authors concluded that both photocatalysts provide a higher rate of near-UV photon absorption and a higher acetone photodegradation rate [2,14], with optimum TiO_2 loadings conditions. Similarly, Bianchi et al. (2014) selected four commercial TiO_2 samples: (a) Cristal PC105, (b) Cristal AT-1, (c) Kronos 1077 and (d) Evonik (DP25), for the degradation of acetone, acetaldehyde, and toluene [55]. Furthermore, Haghighatmamaghani et al. (2019) also utilized two additional commercial TiO_2 photocatalysts, designated as PC500 and S5-300A, for the photocatalytic oxidation of several VOCs such as 2-propanol, 1-butanol, n-hexane, octane, toluene, and others [56,57].

Other authors like Wang et al. (1997) and Barakat et al. (2014) also employed commercial TiO_2 (DP25) to investigate the heterogeneous photocatalytic degradation of trichloroethylene (a widely industrially emitted compound) in a packed bed reactor by coating glass beds with TiO_2 [69]. Barakat et al. (2014) used a plasma reactor loaded with TiO_2 for the complete oxidation of acetone and isopropanol [70].

2.2. Synthesis of TiO_2-Based Photocatalysts

In the last few years, one can report that there have been important improvements in photocatalysts for air treatment for the removal of organic pollutants. In this respect, Sun et al. (2011) prepared a 1% Pt/N-TiO_2 photocatalyst by using a modified sol-gel method. This material responded well to visible light and room temperature, photo-oxidizing several VOCs including ethanol, isopropanol, toluene, and *n*-hexane [58]. Similarly, Moon-Sun et al. (2011) synthesized carbon-doped TiO_2 films, demonstrating the value of an increased specific surface area [71]. Other important transition metals such as iron-III (Fe^{3+}) and none-metals like sulfur (S) were also studied for the doping of TiO_2. For example, Christoforidis et al. (2012) prepared Fe- and S-doped TiO_2 and Fe/S co-doped TiO_2 by chemically modifying a titanium isopropoxide precursor using the microemulsion procedure. This method appears to enhance the photocatalytic activity of single- and co-doped TiO_2 (anatase) under both UV and sunlight irradiation for toluene degradation [59].

Sirivallop et al. (2020) employed an in-situ solvothermal method to prepare four different photocatalysts: (1) TiO_2, (2) N-doped TiO_2, (3) Ag-doped TiO_2 and (4) N/Ag co-doped TiO_2. This resulted in more effective photocatalytic materials for the degradation of gaseous ammonia (NH_3) under visible light-emitting diode (LED) irradiation [11]. Similarly, Yang et al. (2010) prepared a series of N-doped anatase TiO_2 photocatalysts active under visible light [72]. Other authors like Pham et al. (2015) used porous polyurethane (PU) to immobilize a control volume of V-dopant precursor of ammonium metavanadate (NH_4VO_3) and TiO_2, synthesizing in this way a new V-doped TiO_2/PU photocatalyst. This method was shown to be effective for the photocatalytic removal and mineralization of toluene under visible light and room temperature [60]. Gurulakshmi et al. (2012) also used NH_4VO_3 as a dopant precursor to prepare a new V_2O_5/S-TiO_2 (x) photocatalyst by the sol-gel and wet impregnation methods. This new material displayed significantly enhanced visible-light absorption and photocatalytic activity [61].

Almomani et al. (2020) developed a cobalt (Co) co- doped TiO_2 with a sol-gel method, using a Cobalt (II) acetate $Co(CH_3CO_2)_2$ precursor. This semiconductor significantly improved the toluene photocatalytic oxidation under visible light [62]. Huang et al. (2015) also employed a sol-gel method to prepare new photocatalysts doped with various transitional metals (Mn, Co, Ni, Cu, and Fe). These semiconductors, for instance, used manganese (II) acetate $Mn(CH_3CO_2)_2$ and other metal acetates as dopant precursors. Among the prepared photocatalysts, Mn/TiO_2 achieved the highest benzene oxidation under VUV irradiation [63]. Li et al. (2005) used a spray pyrolysis technique to manufacture well-defined size and composition morphologies using N-F-co-doped TiO_2. Those powders were synthesized from a mixed liquid solution containing $TiCl_4$ and NH_4F. After this step, the mixture was atomized by a nebulizer, forming droplets that passed through high-temperature tubes under vacuum to generate the visible-light-driven photocatalytic powder [73].

To date, even though there is a good number of new and enhanced photocatalysts, there is still a need to find the most appropriate semiconductors that could be successfully implemented in scaled-up VOC conversion industrial processes.

3. Photocatalytic Reactors for Air Treatment

Due to the significant increase in building indoor pollution, interest in technologies for the conversion of VOCs has grown. However, and in order to facilitate kinetic modeling, Quantum Yield evaluations and the development of photocatalytic reactors for air treatment scale-up, it is recommended to have (a) a large irradiated surface area, (b) a homogeneous and uniform reactor light-irradiation, (c) light-absorption to promote e^-/h^+ formation, (d) good airflow distribution and (e) minimum air pressure drop. On this basis, the photocatalytic reactors can be classified according to their features: (1) type of irradiation, (2) position of light sources, and (3) photocatalyst deposition method [10].

Thus, and to address this matter, several photocatalytic reactor configurations and light sources are described in this literature review, as well as their respective performances in the degradation of different organic compounds.

3.1. Type of Irradiation

For a photocatalytic reactor to be commercially viable, sunlight is a preferable energy source in principle, as it is readily available, as reported in Figure 2. However, most of the experimental data reported in this review were produced using an assortment of synthetic light sources, including a limited fraction of the sun spectrum.

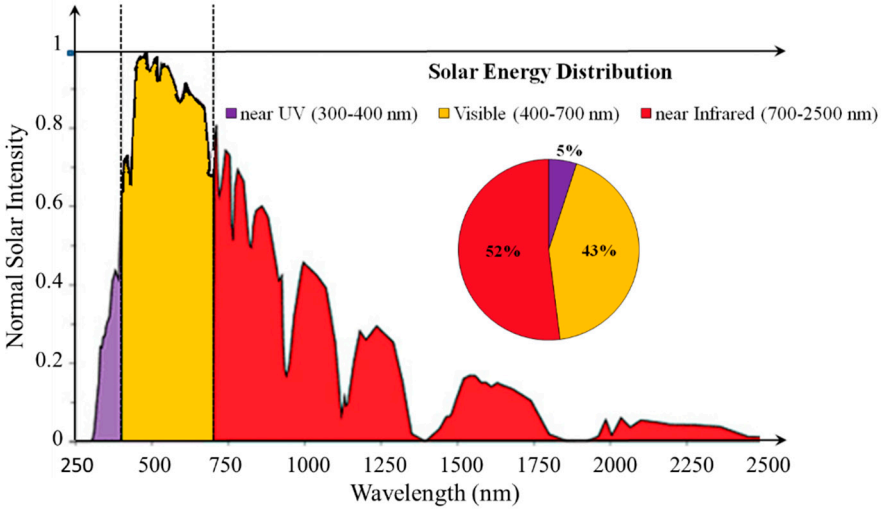

Figure 2. Spectrum distribution of natural solar energy [74].

In this respect, photocatalytic air pollutant degradation is strongly dependent on both the semiconductor band gap and the photon flux (energy per unit area), as well as on the exposed semiconductor surface. It seems that ultraviolet and near-UV light are the preferred radiation sources, given the higher energetic photons produced. Table 2 reports the different types of commercial lamps commonly used for the photocatalytic conversion of organic pollutants in air and water, and for hydrogen production.

Table 2. Different types of light sources employed in photocatalytic reactors for air, water and hydrogen production processes.

Reference	Year	Lamp Type	λ = Wavelength (nm)	Nominal Output Power (W)
[2,38]	1999 & 2002	Peng-Ray® Mercury UV	300 to 410	16
[75]	2007	Philips TL 4W/08 F4T5/BLB	300 to 410	4
[76]	2008	Philips HPK Mercury UV	200 to 600	125
[58]	2011	Philips MSR 575/2 10H metal halide	≈240 to 800	575
[77,78]	2011 & 2013	Philips UV PL—L-40	300 to 400	40
[61]	2012	Tungsten	410 to 800	500
[79]	2013	VUV & UVC Low-pressure mercury (Ster-L-Ray®, Atlantic Ultraviolet Corp.)	150 to 280	18.4
[55]	2014	Jelosil HG 500 halogen	315 to 400	500
[80]	2014	Fluorescent domestic energy-saving light	-	13
[81]	2016	GaN UV-LEDs	376 to 387	≈20
[12]	2016	Polychromatic EIKO Global	325 to 410	15
[17,18]	2013 & 2019	USHIO Blacklight Blue (BLB)	340 to 410	15
[11]	2020	Visible LED	-	16
[19]	2020	Philips mercury visible-light	300 to 700	15

3.2. Position of Light Source

In photocatalytic reactor design and performance, one can see that photoreactors are conditioned by both the position and the location of the incident light sources. On this basis, one should consider (a) the single-lamp annular unit, and (b) the multi-lamp annular unit. These tubular reactor configurations, as described in Figure 3a,b, show an improved photon absorption, with transmitted photons being transported through inner or outer TiO_2 deposition films [82]. These reactors provide symmetrical irradiation, facilitating the calculation of macroscopic irradiation energy balances [12,18,19,33,44].

Furthermore, a photoreactor type with an asymmetrical geometry also allows one to place the reactor light at different locations, as one can see in Figure 3c,d. However, this type of asymmetrical irradiation makes the evaluation of absorbed radiation much more complex [78,83–85].

Thus, while as described in Figure 3a–d photocatalytic performance shows the importance of photon flux irradiation patterns, it is important to state that the photocatalytic reactor efficiency also depends on how the photocatalysts are available on the irradiated surfaces.

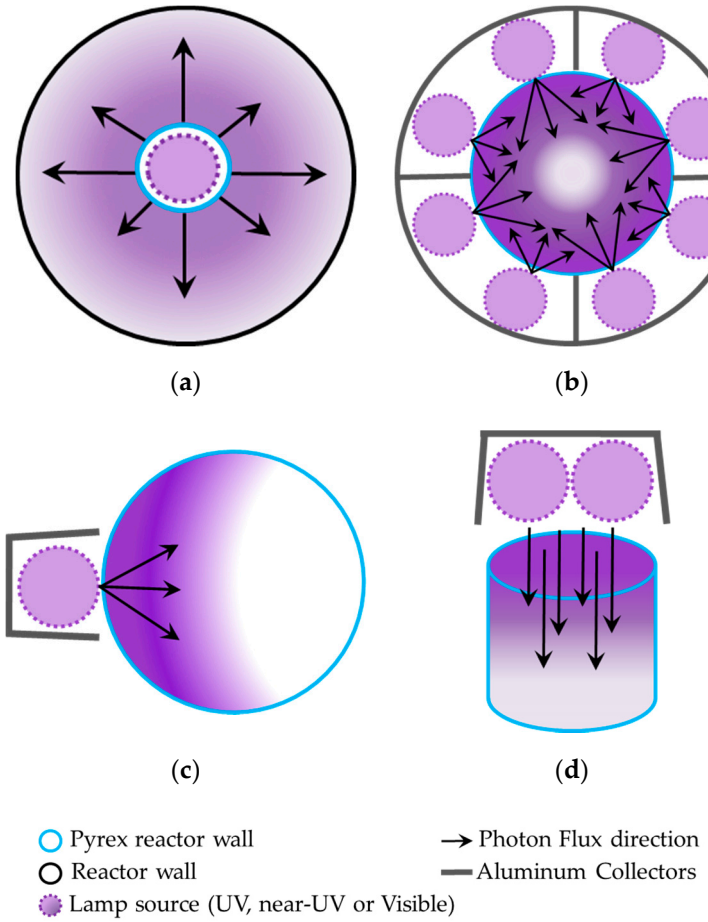

Figure 3. Representation of photocatalytic reactors with lamps placed at different positions: (**a**) internal-annular radial irradiation, (**b**) external-annular radial irradiation, (**c**) external-sided radial irradiation, and (**d**) top axial irradiation. These tubular reactors can also be implemented using rectangular geometries [11,22,79,80].

3.3. Photocatalysts Deposition Methods in Photo-Air Reactors

The study of photocatalyst deposition methods on support surfaces is important to obtain high-performing photochemical reactors. These methods facilitate the photocatalysts' stability, durability, and surface bonding. Thus, a proper deposition method could allow one to create simple and cheap coatings on complex geometries [29]. Moreover, if properly selected and implemented, these methods could effectively help in determining the acceleration of the reaction rate by reducing the irradiation time for the photoconversion of organic pollutants. Table 3 reports different mesh types and common techniques utilized for the immobilization of TiO_2.

Ibrahim and de Lasa (2002) studied a photocatalyst deposition method on a fibrous glass mesh. This fiberglass mesh required a pretreatment for the removal of the protective surface coating (meta-acrylate-chromic) involving several steps: (a) first, the mesh was soaked in a bath of nitric acid solution (70 wt.% HNO_3) for 24 h; (b) then, it was rinsed with de-ionized water; (c) lastly, it was dried at 100 °C for 3 h, which helped with the removal of the coating precursor. After the completion of these steps, the pretreated mesh was brush-painted with a TiO_2 suspension in order to coat the mesh fibers. Then, TiO_2 impregnation was followed by 8 h of drying time to secure water removal [2].

Table 3. Comparison of photocatalyst deposition methods using different types of supports.

Reference	Year	Immobilization Deposition Method	Material Type	Total Area (cm^2)	Mesh Open Area (%)	Photocatalyst Loading (g/cm^2)
[2]	2002	Spread Coating	Fibrous Glass Mesh	510	-	-
[28]	2006	N_2 Spray Coating	Non- Woven Dry Polyester Fabric Mesh	50	HVAC Filter	0.24 ± 0.01
[86]	2008	Galvanostatic Anodization of thin TiO_2 Films	Metallic Titanium Plate	100	-	-
[87]	2009	Dip-Coating	Nonwoven Cellulose-Fiber Tissue	25	-	≈0.093
			Quartz Plate			≈0.025
[88]	2014		304 SS Woven Wire Mesh	214	52	≈0.027
[89]	2015		Cellulose Acetate Monolithic Structure	806.4	-	≈0.0015
[12]	2016	Air Assisted Spray with Automatized Spinning (TiO_2-ASS-ASC)	304 SS Woven Wire Mesh	1042	36	2.2
[90,91]	2010 & 2017	TiO_2 Liquid Deposition	U-VIX TiO_2 Mesh	50	-	≈5.41
[11]	2020	Brush Painting	304 SS Woven Wire Mesh	700	52	1.5 ± 0.5

Garcia-Hernandez et al. (2012) later suggested that an upgraded impregnation deposition method on a woven wire stainless steel (SS) mesh would be valuable. This method consisted of brush spreading a sonicated TiO_2 slurry on a woven wire SS mesh, followed by drying [8]. Similarly, Haghighatmamaghani et al. (2019) coated TiO_2 on a nickel filter surface using a pipetting method and then drying it at 80 °C for 12 h [56]. These DP25 coated meshes displayed high photocatalytic conversion of acetone [2,12], isopropanol [92,93], and hydrocarbon compounds (i.e., alkanes and BTX) [25,38,77,78] and other VOCs [14,15,20,23,94] photodegradation. Despite these advantages, new methods with better homogeneous coating control were claimed to be required.

A different approach to support TiO_2 on an optical fiber was proposed initially by Ollis and Marinangeli (1980) [95] and further optimized by Peill and Hoffmann (1995) [23]. This method consisted of coating a stripped section of an optical fiber (3M Power-Core FT-1.1-UMT) with DP25 (TiO_2). The coating was applied to the stripped section by inverting the bundle and pipetting a solution, followed by air-drying. Finally, the stripped section was heated to 300 °C while the unstripped section was heated to 110 °C for 1 h. This technique allowed light absorption efficiencies of 95% and the direct measurement of light fluxes for Quantum Yields calculations [23].

Verbruggen et al. (2011) studied an immobilization technique involving a one-step suspension coating on glass beads in a packed bed reactor. This method involved washing 2 mm glass beads with ethanol, and then drying them overnight at room temperature. Later, TiO_2 powder was mixed in ethanol to be sonicated for 30 min. Following this, the glass beads were coated using different loadings of this mixture up to 1 wt.% TiO_2. Then, they were air-dried for 15 min. Finally, the coated glass beads were oven-dried at 65 °C for 2 h. According to the authors, this method offers a convenient and versatile alternative compared to using photocatalytic pellets in the photodegradation of ethylene [96]. Furthermore, Hachem et al. (2001) coated glass plates (48 cm^2) with 4 g/L of DP25 suspension. This was helpful to obtain thin deposits with an average of 10 microns optimal film thickness [97].

Lugo-Vega et al. (2016) developed an air-assisted spray coating unit as shown in Figure 4, with an automatized spinning method (TiO_2-AAS-ASC). This method led to a high TiO_2 dispersion over a 304 woven wire SS mesh (55.4 cm by 34.7 cm). The TiO_2-AAS-ASC method consisted of spraying a rotating cylindrical woven wire stainless-steel mesh with a nozzle air gun. Using this device, the stainless-steel mesh was uniformly covered, with TiO_2 particles being suspended in a water slurry. The set target distance of the gun to the mesh was 30 cm. The drum rotation was 12 rpm and the jet air pressure was 20 psia. The coated mesh was dried at room temperature for 24 h [12]. A similar spray coating technique was applied by Han et al. (2012) on a 10 cm by 5 cm by 0.3 cm nonwoven polyester filter

mesh. The mesh was pre-washed in an ultrasonic washer with a 0.5% nonionic agent during 15 min. After this step, it was rinsed with Milli-Q water, followed by sonication for 15 min. Then, it was washed with acetone and dried in a N_2 flow at room temperature. In addition, the mesh was spray-coated with a mixture of DP25 and Ludox AS-40 (binder agent) using a Navite F-75 G air gun with 65 psia of pressure at a 15 cm distance to obtain a uniform coating. Finally, the mesh was cured at 60 °C for 3 h to stabilize the coating [28,98].

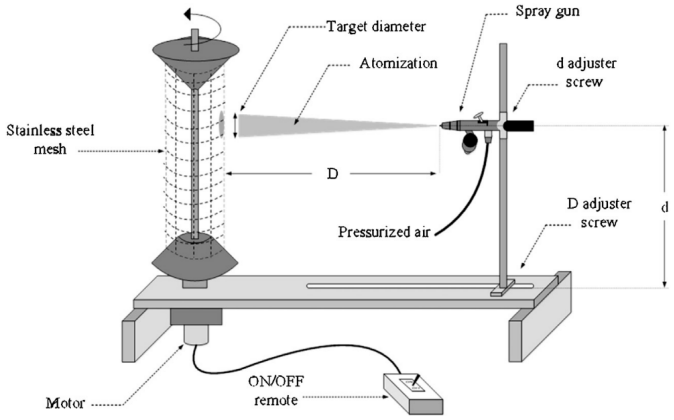

Figure 4. Representation of the automatized spray coating (ASC) system developed by Lugo-Vega et al. (2016) for the TiO_2-AAS-ASC method [12].

Sirivallop et al. (2020) proposed a variation of the Lugo-Vega et al. method [12], using a cylinder of 304 stainless steel (SS) woven wire mesh with a total area of 700 cm^2 and a 52% open area. This mesh (or substrate) was immersed in a diluted nitric acid solution for 1 min and wiped with acetone and ethanol. It was then dried at 100 °C for 3 h. Following this step, the mesh was coated with a brushing technique and a binder of poly (acrylic acid). Then, the mesh was dried at 80 °C for 2 h to achieve the photocatalyst particle immobilization [11].

A different dip-coating method was implemented by El-Kalliny et al. (2014). This technique used 304 SS woven wire mesh with a 214 cm^2 of total area and a 52% open area. The uncoated SS mesh was first rinsed with deionized water and then dried with air. Following this step, it was cleaned with ethanol and methyl ethyl ketone, and dried further at 125 °C for 24 h. The TiO_2 was immobilized on the mesh by horizontal dip-coating for 1 min (the number of TiO_2 dips and loads varied depending on the film thickness applied). Then, the coating films were dried at 100 °C for 15 min. After this, they were calcined at 225 °C for 15 min to obtain an optimal adhesion of the catalyst film [88]. According to Herrmann et al. (1996), dip-coating can also be applied by immersing plates or meshes in a solution of titanium tetraisopropoxide ($Ti(OCH(CH_3)_2)_4$). Either the meshes or the plates are removed from the solution at a constant rate. Then, they are dried in air for a few seconds until white cloudiness appears on the mesh. This occurs given the alcoholate hydrolysis on the adsorbed layer, which is induced by the ambient air humidity. This coating process was repeated until the desired TiO_2 film thickness was reached. Finally, the support was calcined at 400 °C for 2 h. This last step combusted the alcohol precursor and desorbed the CO_2 and/or any other carbon impurities present in the supporting material [99].

The deposition of TiO_2 via a sol-gel method is another common immobilization method used to coat surfaces, including glass [100], quartz [101], metallic plates [102,103], ceramic foams [80] and cotton fabrics [104] with a film of colloidal TiO_2. Harizanov and Harizanova (2000) developed a sol-gel process to stabilize xerogel colloidal TiO_2 films on quartz. This coating method consisted of the polycondensation reaction and the hydrolysis of the suspension containing an organometallic precursor. This was followed by applying a stabilization and dip-coating technique. After this step, the photocatalyst supports were dried at 100 °C during 12 h, and calcined at 450 °C for 5 h, until an optimal TiO_2 film thickness was obtained. One can observe that the resulting film consisted of

nanocrystalline anatase with high optical quality [102]. Given that sol-gel methods were reported to be adequate for fused silica or mineral glasses, at 300 °C or above, Langlet et al. (2002) deposited TiO_2 films on thermally sensitive (<150 °C) polymer supports. These supports consisted of polycarbonates and poly-methyl-methacrylates. A good photocatalytic decomposition of malic acid using anatase films with high crystallinity was obtained [105]. Furthermore, it was determined that sol–gel techniques can also help to prepare porous TiO_2 pellets with high surface areas (≥150 m^2/g), which can be placed in fixed-bed photocatalytic reactors [76,82,103]. For example, Yamazaki et al. (2004) used TiO_2 pellets for the degradation of chlorinated ethylene in a tubular-packed photoreactor [106].

Harizanov et al. (1996) also considered chemical vapor deposition (CVD) on a glass support. This research group used $W(CO_6)$ as a precursor. Different gas atmospheres and temperatures (400 to 600 °C) were utilized in the preparation of CVD-W films. These films were claimed to have a high transmission of solar irradiation [107]. Rachel et al. (2002) introduced the fixation of TiO_2 on solid supports (glass, cement, and red brick) and inorganic fibers, using different techniques such as sol-gel dip-coating and sputtering. According to these authors, the fixation of TiO_2 on inorganic fibers provides good photocatalytic activity for the transformation of benzene into sulfonic acids [108].

Despite the progress achieved, nowadays different research groups are still attempting to achieve an optimal semiconductor deposition. This may lead to coatings with high photoactivity efficiencies of special potential value when using visible light for the inactivation of viruses. It is envisioned that these semiconductor coatings should be developed for industrial and commercial large-scale applications.

3.4. Experimental Photocatalytic Air Reactors for the Photodegradation of Organic Pollutants

There are two Photo-CREC-Air Reactors originally designed by Ibrahim et al. (1999 and 2002), which were proposed to investigate toluene and acetone degradation. These reactors were laboratory-scale closed-loop units of 65 L and 14.7 L, respectively. Both reactors also included (i) a Venturi section with either Degussa P25 or Hombikat UV-100 (TiO_2) impregnated on a wire mesh basket, (ii) a heating plate, (iii) a fan, (iv) sampling ports, and (v) external lamps of 4 W (Pen-Ray®), symmetrically placed around the reactor and housed inside reflectors (see Figure 5a,b). During near-UV irradiation, each unit configuration reached: an ~38% conversion of toluene (13 $\mu g/cm^3$) in 18 h and an ~99% photodegradation of acetone (40 µL solution) in 12 h [2,38].

A similar recirculation closed-loop system (refer to Figure 5c) was later designed by Héquet et al. (2017). This is a 420 L reactor with only 1.3% of the volume corresponding to the PCO section. This PCO section contains a honeycomb section, which provides a homogeneous airflow distribution. It also contains two 18 W UVA UV fluorescent tubes, placed inside the filter folds of the photocatalytic module. The filter folds are composed of a photocatalytic fibrous support (a mixture of cellulose, polyester and polyamide) which is coated with TiO_2 in a SiO_2 binder [84].

In further steps and based on preliminary experimentation and CFD available tools, the annular mesh-coated Venturi-reactor was upgraded [2,9,13,16,31]. The redesigned PCAR, as shown in Figure 6, is a 55.1 L scaled-up reactor with a closed-loop unit that provides an effective interaction between the fluid and the solid phase. In the PCAR, air recirculates using a GASP gas blower and is pumped into a SS Venturi section and then driven into the photoreaction section. Furthermore, this unit operates at close to isothermal conditions (~44 °C), with air being cooled to 5–10 °C, before reentering the blower.

The photoreaction section consists of eight (8) outer near-UV lamps (325 to 380 nm), each having a 15 W nominal power. Lamps are placed in pairs inside lamp-holders which are distributed equally around the circumference of an inner cylindrical quartz glass tube. A TiO_2-coated mesh is supported by a bullet nose bottom, located inside the cylindrical quartz glass tube. This design provides in the reactor section both mesh irradiation and lengthwise gas crossflow from the annular region to the interior of the mesh. The PCAR also allows the determination of macroscopic irradiation energy balances permitting incident, transmitted and reflected light radiation measurements [12,14]. Lugo-Vega et al. (2016) reported that this photoreactor can completely mineralize acetone in air (45 µmol/L), after ~1.6 h of exposure to near-UV irradiation, with a 1 wt.% TiO_2 photocatalyst loaded via the AAS-ASC method [12].

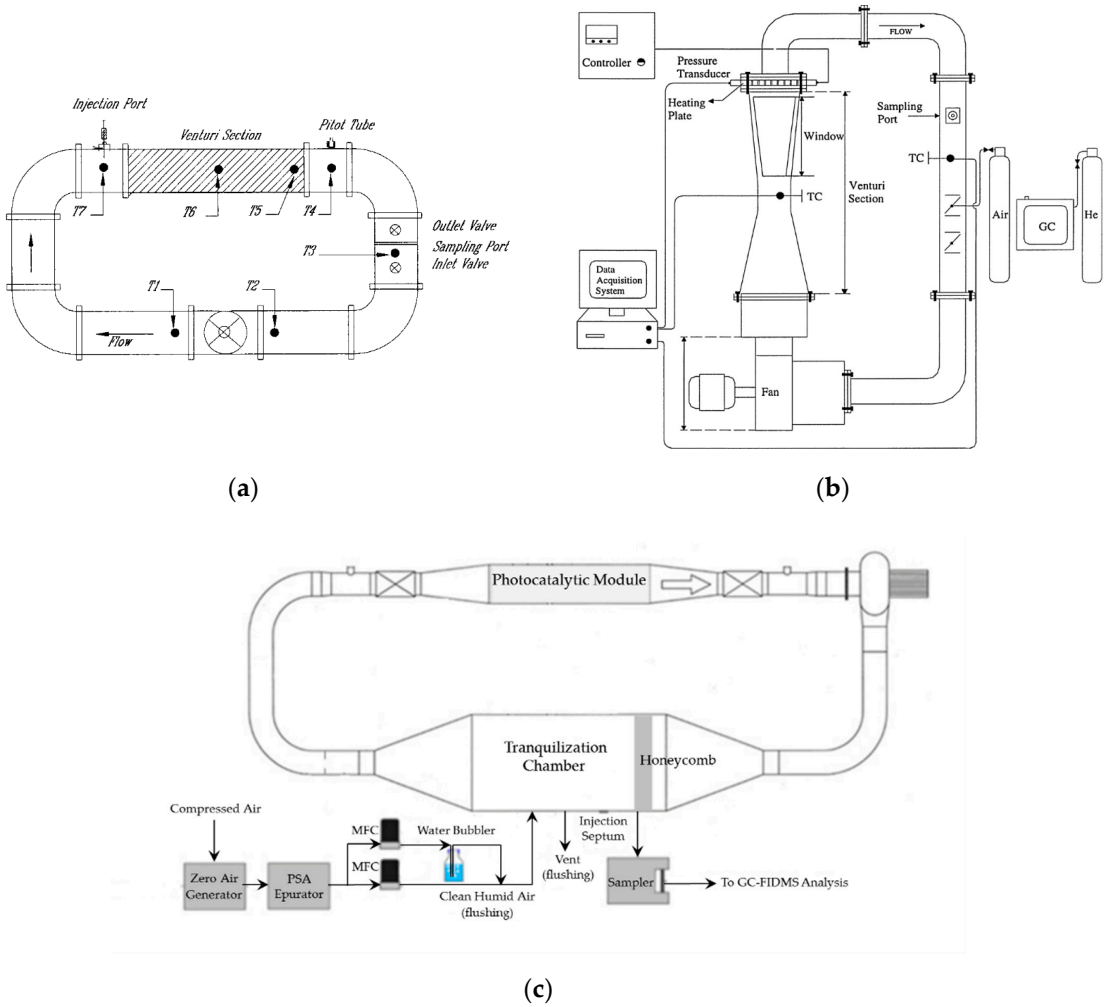

Figure 5. Schematic representation of three experimental closed-loop reactors: (**a**) Photo-CREC-Air Reactor (PCAR-1999 model) [38], (**b**) PCAR-2002 model [2], both designed by Ibrahim et al., and (**c**) closed-loop 2017 model designed by Héquet et al. Diagrams are reproduced with permission [84], MDPI; published by Molecules, 2017.

Imoberdorf et al. (2005) studied the tetrachloroethylene photocatalytic degradation in a photoreactor for air treatment, as shown in Figure 7a–c. These authors used a TiO_2-coated "vertical" borosilicate glass plate, positioned in the same direction of the gas flow. Figure 7a,b show the unit components: (1) a gas inlet, (2) a flow homogenizer, (3) acrylic windows, (4) a photocatalytic plate section, (5) an opaque film, (6) 14 near-UV lamps (black light types) and (7) a gas outlet. Figure 7c describes the components of the process flow diagram: (1) the combined tetrachloroethylene and airflows, (2) the airflow, (3) the mass flowmeters, (4) the air humidifier, (5) the heat exchanger, (6) the thermostatic bath, (7) the mixer, (8) the thermo-hygrometer, (9) the sampling device, (10) the photoreactor, (11) the recycle pump, and (12) the gas scrubber. This reactor with a TiO_2-coated plate was operated under a kinetic control regime [83].

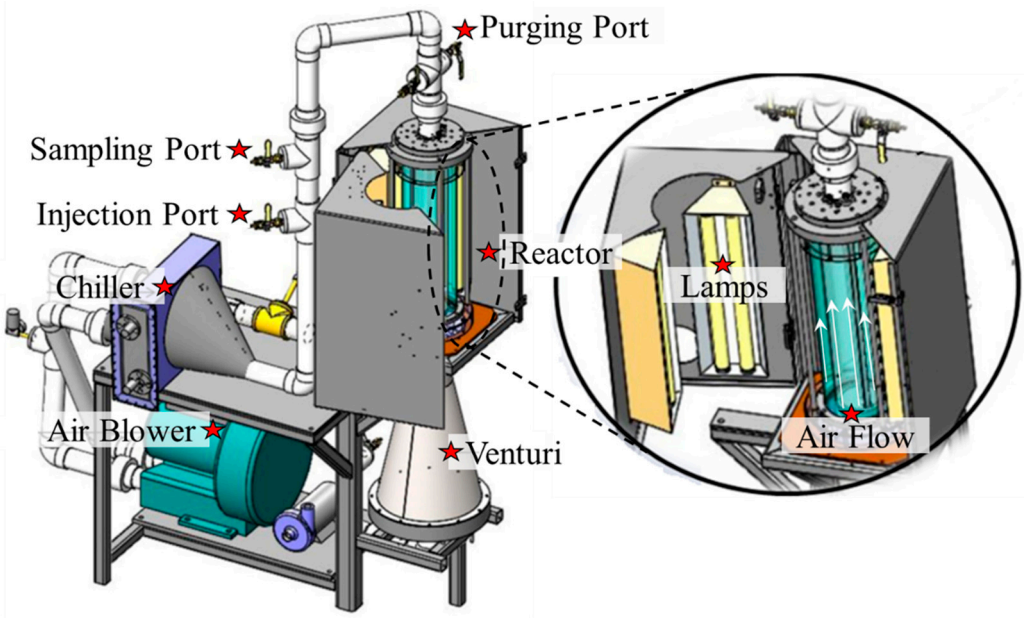

Figure 6. Schematic description of the current version of the Photo-CREC-Air Reactor (PCAR) with an annular mesh-coated Venturi-reactor section.

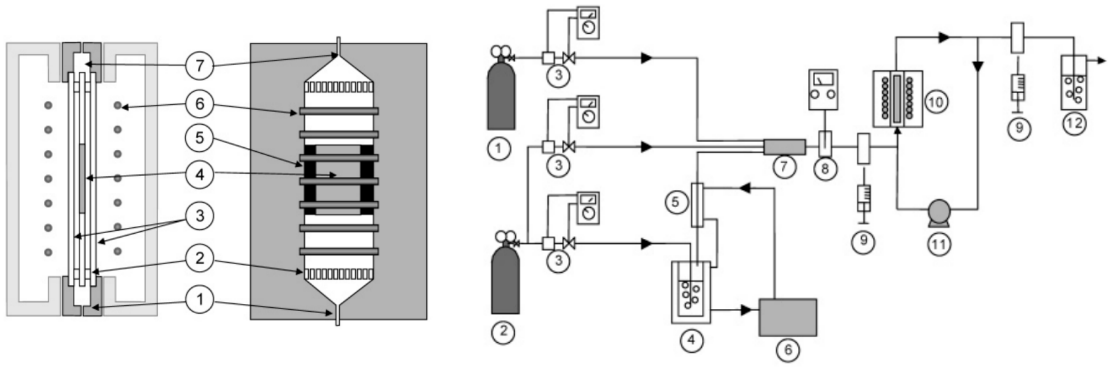

Figure 7. Different views of the photocatalytic air reactor designed by Imoberdorf et al. (2005): (**a**) transversal side cut, (**b**) top, and (**c**) process flow diagrams. Adapted with permission from Reference [83], Copyright (2005), American Chemical Society.

Debono et al. (2011) developed a 120 L laboratory batch reactor for the photocatalytic oxidation of VOCs. The device included (1) a VOC generator, (2) a reaction section with 100 mg of DP25 (TiO_2) dispersed in the lower chamber section, and (3) analytical units for VOC detection and quantification. This reactor was operated at room temperature, with controlled humidity and with nine (9) PL-L-40 Philips near-UV lamps of 365 nm each (see Figure 8). A homogeneous photon flux of 10 ± 1 mW/cm^2 was used. This unit was able to provide a complete photodegradation of toluene following 12 h of irradiation [77,78].

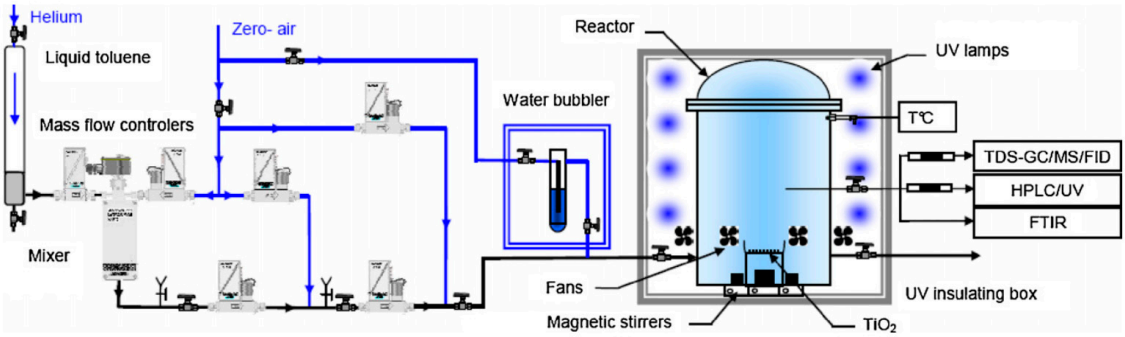

Figure 8. Experimental air treatment setup proposed by Debono et al. (2011). Reprinted from References [77,78], Copyright (2011), with permission from Elsevier.

Dong et al. (2014) customized an experimental 4.5 L continuous flow photocatalytic reactor, with a "horizontal" TiO_2-coated ceramic foam, placed in the same direction as the gas flow. This reactor was specifically designed for operation at ambient temperature under controlled relative humidity and using two (2) domestic energy-saving lamps (refer Figure 9a). Efficiency was demonstrated by eliminating 600 ppb of NO in air at room temperature and close to atmospheric pressure, achieving a 77% NO removal in 30 min as NO_2 and H_2O [80].

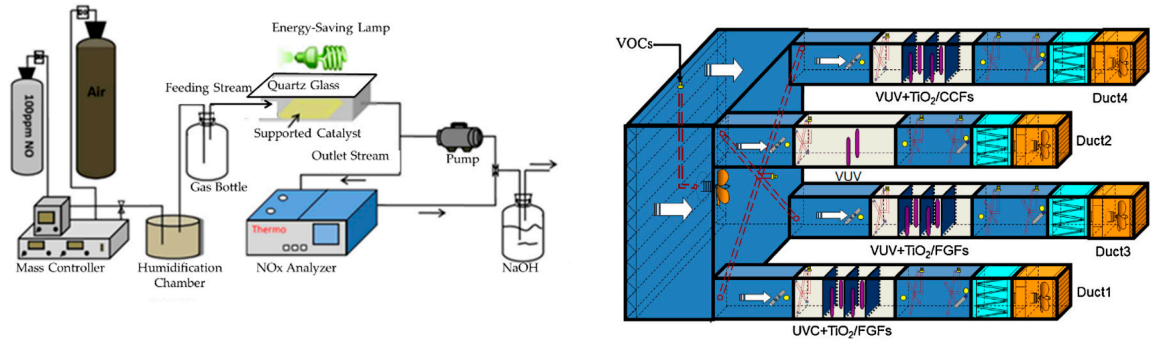

(**a**) (**b**)

Figure 9. Schematic flow diagram of the customized experimental setup for: (**a**) NO degradation under visible light (adapted with permission from Reference [80], Copyright (2005), American Chemical Society), and (**b**) VOC removal under VUV (vacuum ultraviolet) irradiation (reprinted from [79], Copyright (2013), with permission of Elsevier).

Furthermore, Zhong et al. (2013) used a different open-loop photocatalytic reactor design, made of four "parallel" aluminum ducts, with commercial filters coated with TiO_2, situated transversally to the direction of the airflow. This research group studied the oxidation of a variety of VOCs (refer to Figure 9b) by using (i) a vacuum ultraviolet (VUV) lamp and germicidal (UVC) irradiation amounting to 18.4 W per lamp, (ii) a gas mixer feeder, (iii) two commercially available filters for TiO_2 coating, with these being fabricated of fiberglass and carbon cloth fiber, (iv) airflow rates of 255 m^3/h, generated by a radial fan (mounted at the end of each duct) with a speed regulator, and (v) controlled humidity and temperature. This study reported a close to 40% degradation of VOCs for 0.25 to 2 ppm inlet concentrations during 10 h of operation [79,109].

More recently, an experimental photocatalytic air reactor with an 11 L volume (refer to Figure 10) was developed by Xu et al. (2018). The air gas stream was contacted by several nanoporous TiO_2 coated "vertical" plates, placed in the same direction of the gas flow. This photocatalytic unit was equipped with (a) nine (9) low-pressure mercury VUV lamps of 10 W, (b) an ozone removal unit with heating rods and temperature sensors (0–100 °C), and (c) a fan controlling the airflow (~96,000 L/h).

This system exhibited good stability and efficiency, removing about 48% of the formaldehyde and 79% of the total VOCs after 90 min of operation time [85].

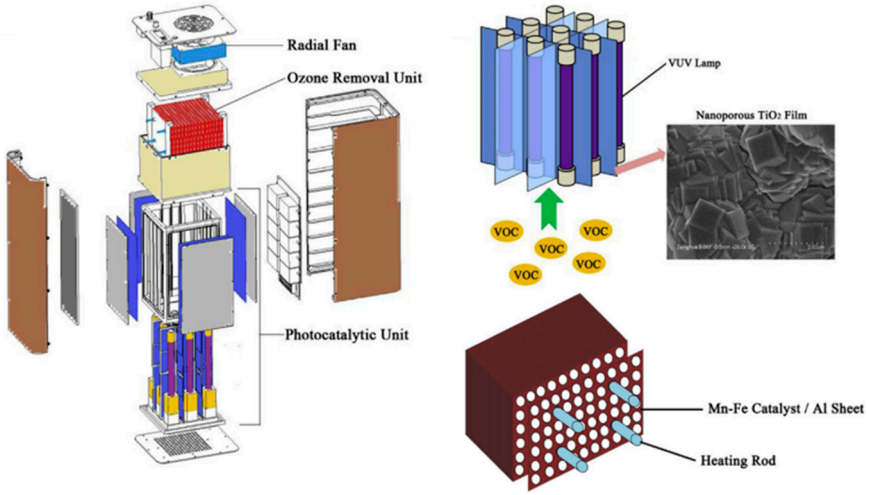

Figure 10. Schematic representation of the VUV (vacuum ultraviolet)-PCO air purifier. Reprinted from Reference [85], Copyright (2018), with permission from Elsevier.

Very recently, a laboratory reactor configuration for air pollution control was reported by Sirivallop et al. (2020). This bench-scale reactor (54 L) operates at room temperature and consists of an "annular" immobilized cylindrical coated-stainless steel wire mesh (coated with an optimal in-situ solvothermal photocatalyst), two visible LED lamps (of 16 W of nominal power), and a fan to circulate ammonia inside a reactor box (refer Figure 11). This reactor configuration achieved an ~38% photodegradation of NH_3 (30% aqueous solution) into N_2 and H_2O during using 5% N/Ag co-doped TiO_2 photocatalyst under 6 h of LED irradiation [11].

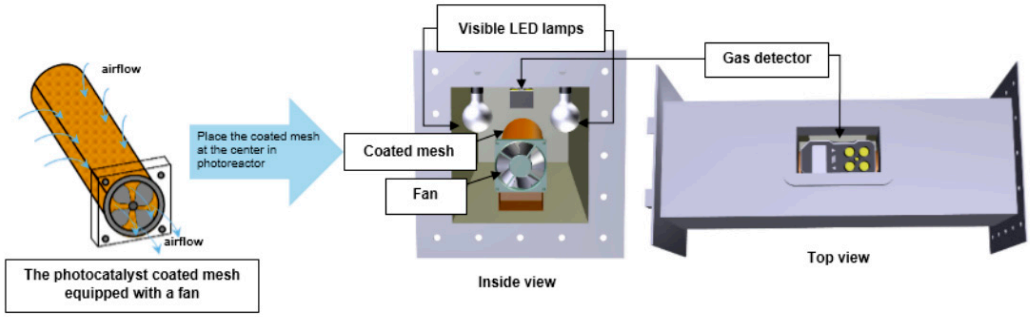

Figure 11. Schematic illustration of the annular coated reactor with LED lamps and a gas detector for NH_3 decomposition. Reproduced with permission from Reference [11], MDPI; published by Catalysts, (2020).

Thus, on this basis, one can conclude that experimental studies which were reported using photocatalytic air purification units, based on diverse possible designs, are still being tested and are under development. In our view, it is worth mentioning that the most advanced photoreactors for this purpose, such as is the case of the Photo-CREC-Air Reactor (PCAR), offer a high degree of uniformly immobilized and irradiated TiO_2, as well as controlled photocatalyst contact with the cross-flows of air. These units offer, in principle, a novel and unique opportunity to manufacture scaled commercial photocatalytic reactors that can efficiently remove indoor pollutants in excess of ~99%.

4. Photodegradation Modeling Studies for Air Treatment Using TiO_2-Based Photocatalysts

In order to progress with photocatalytic oxidation (PCO), there are two issues of major importance: (1) the clarification of photoconversion kinetics and (2) the development of CFD (Computational Fluid Dynamic) modeling. In particular, nowadays, CFD modeling has progressed considerably, as it is able to provide reliable and accurate fluid flow calculations [110].

4.1. Reaction Mechanism Development

During the last two decades, the significant advancement of photocatalytic kinetic models has been reported. These kinetic models are based on bimolecular photocatalytic oxidation reactions occurring between the adsorbed species and oxygen [3]. Salaices et al. (2004) proposed a reaction mechanism involving a parallel-series reaction network (refer to Figure 12), for phenol photoconversion in aqueous media. This model was supported by experimental data (arrowed-lines) and sound assumptions (arrowed-dashed lines) [111]. Furthermore, this model has been used as a groundwork for further kinetic studies in the photoconversion of organic pollutants in water [112–114], air [8,31,33], and for hydrogen production [34,115] at the CREC-UWO laboratories.

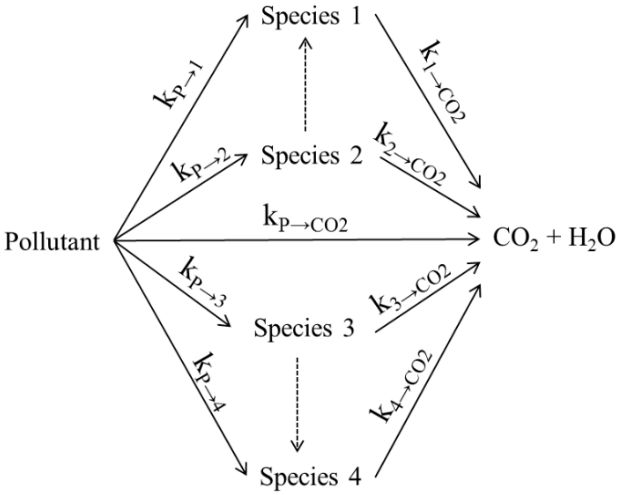

Figure 12. Description of the "parallel-series" reaction network for the photodegradation of organic pollutants based on "observable" intermediate species and CO_2. Note: "k_i" denotes the kinetic constant for each individual reaction step [3]; and the term "Species" refers to intermediate oxygenated species formed during model pollutant conversion.

In particular, it can be mentioned that the CREC-UWO group has led the development of the parallel-series reaction network for air treatment, describing photodegradation of acetone, acetaldehyde, and isopropanol into CO_2 and H_2O when using TiO_2 [8,31,33]. This practical and effective reaction network, based on measurable chemical species, was validated accounting for the variable absorbed photon density at various photocatalyst irradiated site locations. This intrinsic photoreactor characteristic led to both h^+ site and $OH^\bullet$ radical group variability. As a result, the photocatalytic reactor yielded photocatalytic reaction steps which took place with different oxidation extents. This scenario gave: (a) CO_2, from the very beginning of the irradiation period, and (b) other intermediate species, requiring a lower number of $OH^\bullet$ radicals than those for the complete mineralization of the model pollutant.

On the other hand, Imoberdorf et al. (2005), proposed a more complex sequence of elementary reaction steps. This reaction mechanism involved radical species and was considered adequate for the degradation of tetrachloroethylene [84]. The series of postulated reaction steps are summarized in Figure 13.

process	reaction steps	reaction rates
initiation:	$TiO_2 \rightarrow TiO_2 + e^- + h^+$	r_g
	$h^+ + H_2O_{ads} \rightarrow OH^\bullet + H^+$	$k_1[H_2O]_{ads}[h^+]$
	$h^+ + HO^-_{ads} \rightarrow OH^\bullet$	
	$e^- + O_2 \rightarrow O_2^{\bullet-}$	$k_2[O_2][e^-]$
($Cl^\bullet$) generation:	$C_2Cl_{4\ ads} + OH^\bullet \rightarrow C_2Cl_4OH^\bullet$	$k_3[C_2Cl_4]_{ads}[OH^\bullet]$
	$C_2Cl_4OH^\bullet + O_2 \rightarrow C_2Cl_4OHOO^\bullet$	$k_4[C_2Cl_4OH^\bullet][O_2]$
	$2\ C_2Cl_4OHOO^\bullet \rightarrow 2\ C_2Cl_4OHO^\bullet + O_2$	$k_5[C_2Cl_4OHOO^\bullet]^2$
	$C_2Cl_4OHO^\bullet \rightarrow C_2Cl_3OHO + Cl^\bullet$	$k_6[C_2Cl_4OHO^\bullet]$
chain propagation:	$C_2Cl_{4\ ads} + Cl^\bullet \rightarrow C_2Cl_5^\bullet$	$k_7[C_2Cl_4]_{ads}[Cl^\bullet]$
	$C_2Cl_5^\bullet + O_2 \rightarrow C_2Cl_5OO^\bullet$	$k_8[C_2Cl_5^\bullet][O_2]$
	$2\ C_2Cl_5OO^\bullet \rightarrow 2\ C_2Cl_5O^\bullet + O_2$	$k_9[C_2Cl_5OO^\bullet]^2$
	$C_2Cl_5O^\bullet \rightarrow CCl_2O + CCl_3^\bullet$	$k_{10}[C_2Cl_5O^\bullet]$
	$C_2Cl_5O^\bullet \rightarrow C_2Cl_4O + Cl^\bullet$	$k_{11}[C_2Cl_5O^\bullet]$
	$CCl_3^\bullet + O_2 \rightarrow CCl_3OO^\bullet$	$k_{12}[CCl_3^\bullet][O_2]$
	$2\ CCl_3OO^\bullet \rightarrow 2\ CCl_3O^\bullet + O_2$	$k_{13}[CCl_3OO^\bullet]^2$
	$CCl_3O^\bullet \rightarrow CCl_2O + Cl^\bullet$	$k_{14}[CCl_3O^\bullet]$
ending reactions:	$e^- + h^+ \rightarrow$ heat	$k_{15}[h^+][e^-]$
	$Cl^\bullet + M \rightarrow$ products	$k_{16}[Cl^\bullet][M]$
nonradical reaction:	$CCl_2O + H_2O \rightarrow CO_2 + 2\ HCl$	
adsorption:	$C_2Cl_4 + sites \leftrightarrow C_2Cl_{4\ ads}$	thermodynamic equilibrium
	$H_2O + sites \leftrightarrow H_2O_{ads}$	thermodynamic equilibrium

Figure 13. Reaction mechanism for the degradation of tetrachloroethylene as proposed by Imoberdorf et al. (2005). Adapted with permission from Reference [83], Copyright (2005), American Chemical Society.

Yu et al. (2010) also introduced a kinetic model for the photocatalytic oxidation of nitric oxide (NO) [116]. This process is described in Figure 14. This mechanism involves both measurable and non-measurable intermediate radical species.

a) Steps representing the carbon modified TiO_2,

$TiO_2 + H_2O \overset{K_{H_2O}}{\rightleftarrows} TiO_2\text{-}H_2O$

$TiO_2 + O_2 \overset{K_{O_2}}{\rightleftarrows} TiO_2\text{-}O_2$

$TiO_2 + NO \overset{K_{NO}}{\rightleftarrows} TiO_2\text{-}NO$

b) Steps describing the electron/hole generation pairs and the oxidation of NO generated during the hole trapping,

$TiO_2 + h\nu \xrightarrow{\phi} e^- + h^+$

$h^+ + TiO_2\text{-}H_2O \xrightarrow{k_{h^+}} OH^\bullet + H^+$

$e^- + TiO_2\text{-}O_2 \xrightarrow{k_{e^-}} O_2^-$

$TiO_2\text{-}NO + OH^\bullet \xrightarrow{k_{NO}} TiO_2\text{-}HNO_2$

$TiO_2\text{-}HNO_2 + OH^\bullet \xrightarrow{k_{HNO_2}} TiO_2\text{-}NO_2 + H_2O$

$TiO_2\text{-}NO_2 + OH^\bullet \xrightarrow{k_{NO_2}} NO_3^- + H^+$

$TiO_2 + NO_2 \overset{K_{NO_2}}{\rightleftarrows} TiO_2\text{-}NO_2$

c) Final step representing the heat generation due to the electron/hole pair recombination,

$e^+ + h^- \xrightarrow{k_{deg}} \text{heat}$

Figure 14. Reaction mechanism for the photodegradation of NO [116].

Thus, while the present review reports relevant photocatalytic mechanisms, one can observe that researchers are still debating on how to proceed further to obtain kinetics for indoor air purification. It is our view that the "series-parallel" model, first introduced by CREC-UWO researchers [111], provides an excellent approach for describing measurable species concentration changes, as well as a workable method to establish the consumption of $OH^\bullet$ radicals at every step of the photocatalytic conversion, and using stoichiometric equations. It is also anticipated this "series-parallel" kinetic model based on observable oxidized species can help to improve photocatalytic reactor design. This is due to the kinetic model's simplicity and accuracy.

4.2. Adsorption and Kinetic Modeling Development

There are three important kinetic parameters to assess photocatalytic performance: (i) photoreaction rates, (ii) adsorption constants, and (iii) intrinsic kinetic constants. These parameters are

influenced by (a) humidity, (b) temperature, (c) wavelength, (d) radiation intensity, (e) gas velocity, (f) residence time, (g) photocatalyst loading, (h) oxygen and (i) organic pollutant concentration. The variation of any of these parameters can help us to improve the scale-up of photocatalytic processes [3].

Regarding adsorption, a Langmuir adsorption isotherm can be considered to be a suitable expression for the adsorbed species on the TiO_2 at equilibrium [10,34,117,118]. This expression can be represented as follows:

$$\theta_A = \frac{Q_{eq,ads}}{Q_{eq,max}} = \frac{K^A_{eq,i} C_{eq,i}}{\left(1 + K^A_{eq,i} C_{eq,i}\right)} \quad (1)$$

where θ_A stands for the dimensionless surface species concentration, where $Q_{eq,ads}$ and $Q_{eq,max}$ in (mol/g_{cat}) represent the existing and maximum equilibrium adsorption surface concentrations, respectively; where $C_{eq,i}$ (µmol/m^3 or ppm) denotes the equilibrium of species "*i*" in the gas phase concentration, or in the model pollutant concentration; and where $K^A_{eq,i}$ (m^3/µmol or ppm^{-1}) represents the adsorption equilibrium constant. In this respect, only a few studies estimate adsorption constants using independent equilibrium experiments. Adsorption parameters can be assessed using "dark" conditions (without irradiation). This allows for independently calculated adsorption parameters, minimizing in this respect the intrinsic kinetic parameters cross-correlation. Therefore, it is apparent that it is adequate to independently calculate Langmuir adsorption parameters, reducing cross-correlation and, therefore, parameter calculation uncertainty [119–121].

However, in humid air conditions, Maudhuit et al. (2011) established that the classical adsorption model as in Equation (1) cannot be applied. Consequently, a new approximation designated a "Langmuir-multi" model was considered. This model was built and fitted to the experimental data for the adsorption of toluene and acetone. According to their hypotheses, the first part of the curve of the Langmuir equation was kept as Equation (1) for $0 \le C_{eq,i} \le 3$ mmol/m^3 For higher $C_{eq,i} \ge 3$ mmol/m^3 however, the Langmuir-Freundlich Equation (2) was considered for different possible mechanisms accounting [122] for:

$$Q_{eq,ads} = Q_{eq,max-1} \frac{K^{A1}_{eq,i} C_{eq,i}}{\left(1 + K^{A1}_{eq,i} C_{eq,i}\right)} + Q_{eq,max-2} \frac{K^{A2}_{eq,i} \left(C_{eq,i} - C_{eq,Inf}\right)^n}{1 + K^{A2}_{eq,i} \left(C_{eq,i} - C_{eq,Inf}\right)^n} \quad (2)$$

where $Q_{eq,ads}$, $Q_{eq,max-1}$ and $Q_{eq,max-2}$ in (mmol/g_{cat}), represent the existing and maximum equilibrium adsorption surface concentrations; where ($_{-1}$) and ($_{-2}$) are the Langmuir and Freundlich adsorption isotherms, respectively; where $C_{eq,i}$ (mmol/m^3) denotes the equilibrium of species "*i*" in the gas phase concentration or model pollutant concentration; where $K^{A1}_{eq,i}$ and $K^{A2}_{eq,i}$ (m^3/mmol) represent the adsorption equilibrium constants for the Langmuir and Freundlich adsorption equations, respectively; where $C_{eq,Inf}$ (mmol/m^3) stands for the inflection point observed in the adsorption isotherm; and finally, where *n* is the number of adsorption layers.

Regarding reaction rate models, it has been established that organic pollutants are adsorbed at equilibrium on TiO_2 surfaces [71,123–129]. Thus, one has to consider mathematical models, such as the Langmuir-Hinshelwood (LH) kinetics [3,10,14,123,125–128,130–132]. Thus, the general expression of the Langmuir-Hinshelwood equation for batch reactors, with different model pollutants photoconverted in air, is given by:

$$V \frac{dC_i}{dt} = -r_i A \quad (3)$$

$$r_i = \frac{V}{A} \frac{dC_i}{dt} = -\frac{K^A_{eq,i} k_i C_{eq,i}}{\left(1 + K^A_{eq,i} C_{eq,i}\right)} = -\frac{C_{eq,i}}{\left(\theta_{1,i} + \theta_{2,i} C_{eq,i}\right)} \quad (4)$$

where V (m^3) represents the total gas contained in the PCAR; where k_i (μmol/min m^3) represents the equilibrium kinetic constant of species "i"; where r_i (μmol/min × m^2) is the rate of photoconversion of the model pollutant "i", and where A (m^2) is the uniformly irradiated mesh area holding an optimum loading of TiO_2 particles. Furthermore, Equation (4) can also be represented in terms of $\theta_{n,i}$ parameters, where $\theta_{1,i} = 1/K^A_{eq,i}k_i$= (min) and $\theta_{2,i} = 1/k_i$= (min m^3/μmol).

Thus, once the irradiation is initiated, the photocatalytic oxidation of species "i" leads to the formation of intermediate species, that can also be adsorbed on the TiO_2 surface. Then, Equation (4) can be modified to include the formation of one or more kinetically important intermediate species ($\sum K^A_{eq,j}C_{eq,j}$) [8,133–135], as follows:

$$r_i = -\left(\frac{V}{A}\right)\frac{K^A_{eq,i}k_iC_{eq,i}}{(1 + K^A_{eq,i}C_{eq,i} + \sum K^A_{eq,j}C_{eq,j})} \quad (5)$$

Using this approach, Ibrahim and de Lasa (2003) established a kinetic model similar to the one reported via Equation (5). This was the basis of a Photo-CREC-Air Reactor model for VOCs' photoconversion. In Equation (5), adsorption and intrinsic reaction parameters can also be established using a least-square non-linear regression analysis with the related statistical indicators [10].

Vorontsov et al. (2000) reported a different approximation for the complete mineralization of acetone, using platinized titanium dioxide (Pt/TiO_2) as a photocatalyst. The authors employed a variation of an LH equation by considering two types of adsorption sites (surface hydroxyl groups and Ti^{4+} ions) as shown in Equation (6) [136]:

$$r_i = \frac{K^A_{eq,1}k_1C_{eq,1}}{1 + K^A_{eq,1}C_{eq,1}} + \frac{K^A_{eq,2}k_2C_{eq,2}}{1 + K^A_{eq,2}C_{eq,2}} \quad (6)$$

Intrinsic kinetic and adsorption constants have been studied in the technical literature for the photodegradation of common VOCs including acetone, acetaldehyde, toluene, and isopropanol. These studies have also been performed both in bench-scale and scale-up reactors (i.e., Photo-CREC-Air Reactor) and represent a step forward in the implementation of PCO processes. Table 4 reports intrinsic kinetic constants and adsorption parameters, reported by different authors using the previously listed set of Equations from (1) to (6).

It is important to state that while there has been progress in terms of kinetics for photocatalytic reactors, this is still a critical area that deserves further attention. This area involves the successful scale-up of these units, as well as photoreactor unit design performance based on quantum efficiencies.

Table 4. Comparison of adsorption and kinetic constants for TiO_2-based photocatalytic conversion of VOCs.

Ref.	Year	Eq. *	$C_{pollutant}$ (µmol/L)	$K^A_{eq,i}$				k_i	
[120]	1994	1	Blend Acetone + Water: (7.11) + (≈1206)	$K^A_{eq,Ace}$		$K^A_{eq,Wat}$		4.57×10^7 µmol/m^3 min	
				(m^3/mg)					
				0.208		0.0102			
[125]	2007		Blend Toluene (0.173) + Benzene (0.037)	$K^A_{eq,Tol}$		$K^A_{eq,Ben}$		k_{Tol}	k_{Ben}
				(m^3/mg)				10^{-7} (mol/m^2 s)	
				0.24 ± 0.04		0.77 ± 0.44		6.77 ± 0.65	1.56 ± 0.51
[122]	2011	2	Toluene (5×10^{-4})	$Q_{eq,m1}$	$Q_{eq,m2}$	$K^{A1}_{eq,i}$	$K^{A2}_{eq,i}$	-	
				(mmol/m^2)		(m^3/mmol)			
				0.59 ± 0.06	0.41 ± 0.02	0.42 ± 0.05	1.28 ± 0.5		
[31]	2004	4	Acetone (60)	10^{-5} (m^3/µmol)				10^{-4} (µmol/m^3 min)	
				4.5 ± 0.18				2.04 ± 0.001	
			Acetaldehyde (50)	0.71 ± 0.03				0.27 ± 0.02	
[8]	2012		Acetone (49)	4.8 ± 0.09				13.15 ± 0.03	
			Acetaldehyde (320)	0.31 ± 0.04				1.97 ± 1.18	
[118]	2009			10^4 (m^3/mol)				10^{-7} (mol/m^2 s)	
			Pentane (1386)	1.14				1.81	
			i-Pentane (1386)	1.51				1.97	
			Hexane (1160)	1.25				2.16	
			i-Hexane (1160)	1.54				2.48	
			Heptane (998)	2.83				3.03	
			Water (1×10^{-3})	0.00112				-	
[16]	2017	5	Acetone (50)	10^{-5} (m^3/µmol)				10^{-4} (µmol/m^3 min)	
				4 ± 1				2.7	
			Acetaldehyde (50)	9 ± 2				2.4	
[136]	2000	6	Acetone (8608)	$K^A_{eq,1}$		$K^A_{eq,2}$		k_1	k_2
				10^{-3} (ppm^{-1})				10^{-10} (mol/s)	
				88 ± 0.7		0.97 ± 0.02		23.8 ± 0.4	22.5 ± 0.8
				100 ± 7		0.35 ± 0.2		29.1 ± 2	7.86 ± 2.2

* NOTE: The numbers in parentheses () are the pollutant concentration represented in µmol/L. "Eq." refers to the kinetic model used in each specific study. The number assigned to "Eq." is the same equation reference number also used in the manuscript text.

4.3. Computation Fluid Dynamic (CFD) Development

Computational fluid dynamics is an emerging and efficient tool that allows a better understanding of fluid flow patterns. It is critical to address the analysis, the development and the optimal design of photocatalytic reactors for air or water treatment processes [37,82,137]. Performing hydrodynamic simulations is the first step in the modeling of photoreactors. The Navier-Stokes equations are adequate for calculating the hydrodynamics of single-phase reactor systems. Nevertheless, for multiphase flows, there are two general methodologies: (i) the Eulerian-Eulerian (E-E) model, and (ii) the Eulerian-Lagrangian (E-L) model. In general, E-E models are preferred to solve multiphase flows compared to the E-L models, because of their rigorous computational approach [36].

Romero et al. (2006) reported the application of CFD modeling to the design of a pilot-scale photocatalytic air treatment reactor. This study, considered in the context of Photo-CREC-Air Reactor unit, originally developed by Ibrahim and de Lasa (2002) [2], was valuable to identify potential design issues and then to envisage a modified design with improved irradiation and flow field parameters. The CFD analysis was performed using CFX-5.7.1 (Ansys, Inc., Canonsburg, PA, USA), which is commercial software that uses the finite volume method to solve the discrete forms of transport equations. In this respect, the numerical solution of the Photo-CREC-Air Reactor (PCAR) was developed by using the steady-state continuity and the Reynolds averaged Navier-Stokes equations [13].

CFD simulations, as reported in Figure 15a, allowed our team to establish that in the first PCAR-1 unit there was: (a) a boundary layer separation, downstream from the basket base, caused by the basket sharp edge, favoring a dead volume formation; and (b) poor photocatalyst utilization due to the gas recirculation observed. On the other hand, Figure 15b showed the significant improvements achieved in the PCAR-2 by having (a) uniform near-UV irradiation on the photocatalyst, (b) a more regular flow field and velocities in the annular region, and (c) more uniform gas mass flows and fluid contact times [13].

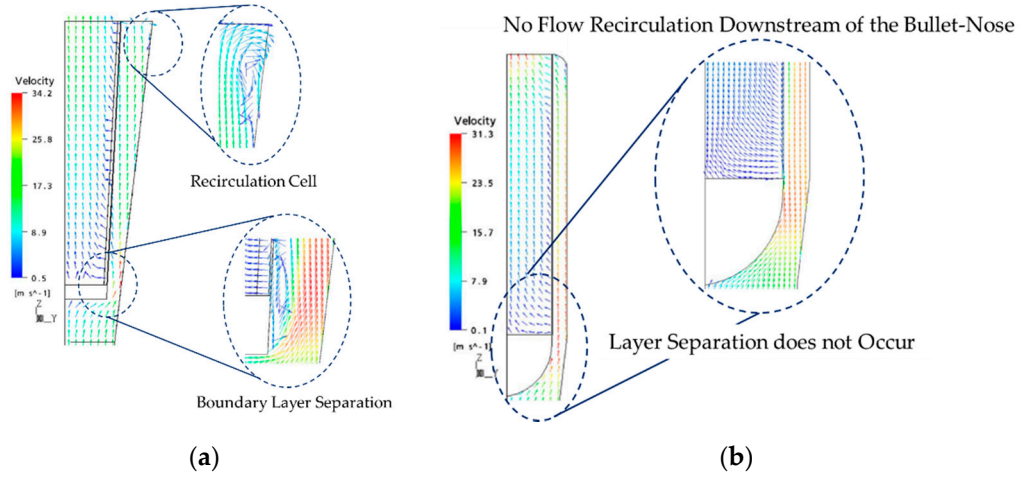

Figure 15. CFD for the velocity field plotted on the YZ-symmetric plane (x = 0) of (**a**) PCAR-1 a rectangular basket and perforate plates [2] and (**b**) PCAR-2 with a bullet nose and cylindrical basket [13].

Later, Romero et al. (2007) also examined the reactor decontamination performance (see Figure 16) using CFX-10 in a continuous mode [9]. This was done by incorporating the acetone kinetic model proposed by Ibrahim and de Lasa (2004) [31]. The CFD governing equations used in this study were

(a) Reynolds-averaged mass,

$$\frac{\partial \rho}{\partial t} + \nabla \bullet (\rho U) = 0 \tag{7}$$

(b) Momentum,

$$\frac{\partial \rho U}{\partial t} + \nabla \bullet \{\rho U \otimes U\} = -\nabla \bullet \{\tau + \tau_t\} + S_M \tag{8}$$

(c) Acetone transport,

$$\frac{\partial C_{Ac}}{\partial t} + \nabla\bullet\{UC_{Ac}\} = \nabla\bullet\left(\rho(D + D_t)\nabla\left(\frac{C_{Ac}}{\rho}\right)\right) + S_C \quad (9)$$

where ρ is the fluid density (kg/m^3); where ∇ stands for the gradient vector of x, y and z coordinates; where t is time (s); where U stands for fluid velocity vector (m/s); where $\otimes$ is the tensor product; where τ and τ_t represent the stress tensor and the Reynolds stress tensor (N/m^2), respectively; where S_M is the momentum source/sink term (kg/m^2 s^2); where C_{Ac} stands for the acetone concentration (kg/m^3); where D is the diffusivity of acetone in air (m^2/s) and was estimated with the method developed by Fuller et al. [138]; where D_t represents the eddy diffusivity (m^2/s); and where S_C is the acetone source/sink term (kg/m^3 s).

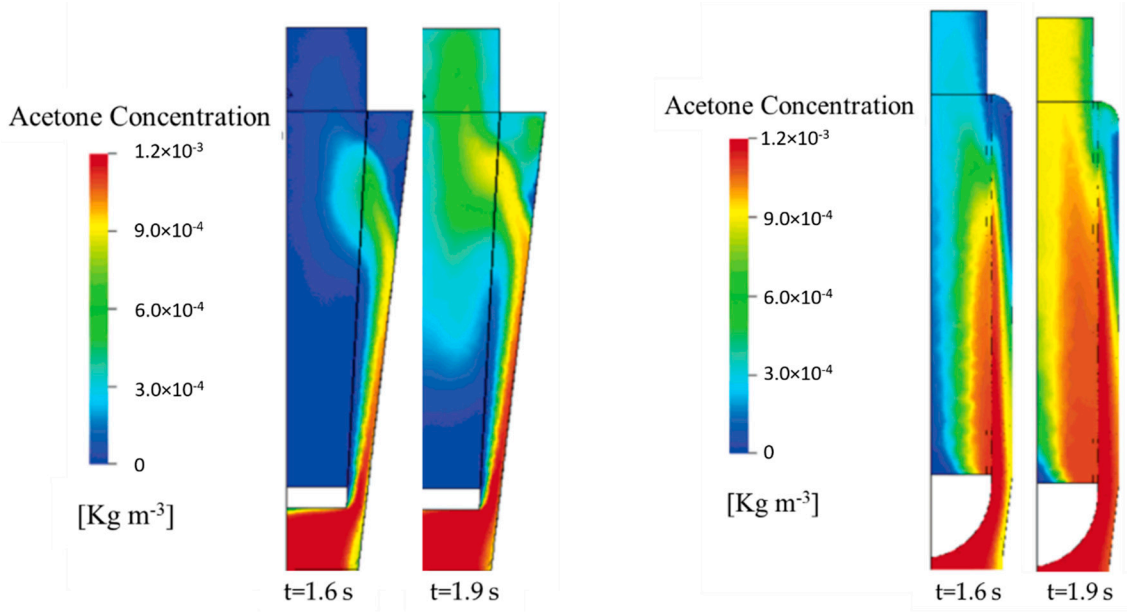

(**a**) (**b**)

Figure 16. Snapshots of acetone concentrations plotted on the YZ-symmetry plane at t = 1.6 and 1.9 s for (**a**) PCAR-1 and (**b**) PCAR-2 [9].

The Reynolds stresses, represented with the τ_t term in Equation (8), were calculated with the *k-w* Shear Stress Transport (SST) turbulence model [9]. Furthermore, local density variations were calculated using the ideal gas law and assuming pressure domain ambient conditions to be 1 atm. Furthermore, one should note that the energy equation was not included in the model, given that isothermal operation was assumed, setting the domain temperature to ~25 °C.

The CFD simulation of the PCAR reported in Figure 16 compares two different single-pass photoreactor designs showing that (a) the PCAR-1 displays poor volumetric flow and low acetone conversion; and (b) the PCAR-2 shows a higher acetone photoconversion of 7.8%, which is attributed to a higher near-UV irradiation flux, a larger surface area available for the reaction and improved volumetric flow [9]. These results also show the limitations of the continuous photocatalytic single-pass reactors operation for VOCs' removal.

Vincent et al. (2011) also implemented a CFD model for the photocatalytic degradation of acetone in an annular reactor (refer to Figure 17a). The CFD modeling provided a good description of the plug flow dispersion in the reactor, especially when the Navier-Stokes, the Brinkman, and the convection-diffusion equations were used [35]. Similarly, Degrave et al. (2015) employed the governing stationary equations given by (a) the Navier-Stokes model for the fluid domain and (b) the Darcy-Brinkman model for the porous media. These authors proposed a numerical model at the optical fiber scale to perform

numerical simulations in geometrical domains. It consisted of a representative volume element (RVE) of the photocatalytic surface with periodic boundary conditions. For instance, this method allowed the authors to determine the permeability of the fabric (K), in which the higher the K, the higher the slip velocity (10^{-10} m^2 < K < 10^{-9} m^2). Figure 17b reports the spatial field of the airflow at the interface between the porous fabric and the free flow region [139].

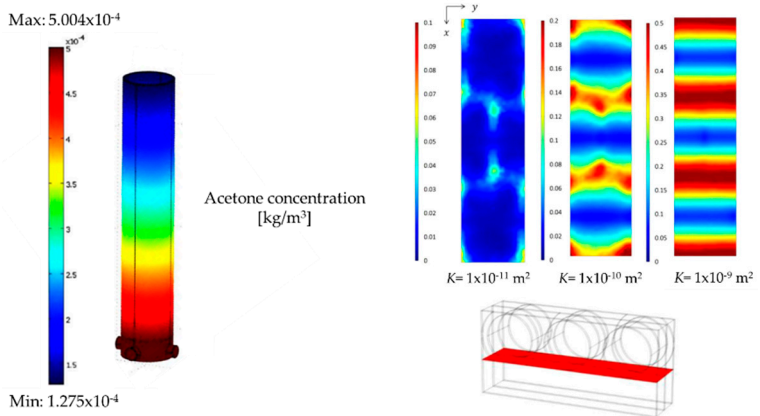

(**a**) (**b**)

Figure 17. (**a**) Variation of acetone inside the annular reactor, $C_0 = 5 \times 10^{-4}$ kg/m^3; (adapted from Reference [35], Copyright (2011), with permission from Elsevier) and (**b**) U_S/U_{Max} ratio between interface slip velocity and the maximum velocity for various permeabilities (K); (reprinted from Reference [139], Copyright (2015), with permission from Elsevier).

On this basis, it is apparent that modeling studies of photocatalytic reactors using CFD must be developed. This will help to improve reactor design and operation, as well as to reduce the manufacturing cost of medium and large-scale systems.

5. Energy Efficiency Studies for Air Treatment Photoreactors

Energy efficiencies in photocatalytic reactors are of critical importance because they establish the performance of a specific design. Nevertheless, their evaluation is still a challenge given: (i) the photocatalyst absorbed irradiation, (ii) the reaction networks (or mechanism), (iii) the kinetic constants (k_i) and (iv) the adsorption constants $\left(K^A_{eq,i}\right)$.

In this review, we summarize some of the most relevant efficiency parameters in photocatalytic processes. We consider both the Quantum Yields (QY or φ) and the Photocatalytic Thermodynamic Efficiency Factors (PTEFs). These parameters help us to calculate the efficiencies of air treatment photoreactors. Table 5 presents data comparisons between quantum efficiencies and PTEFs for different VOCs when a TiO_2-based photocatalysts is employed.

Table 5. Data comparison of quantum efficiencies and PTEFs obtained in different photoreactors employing TiO_2-based photocatalysts for the elimination of various VOCs.

Ref.	Year	Pollutant (μmol/L)	Temperature (°C)	QYs % (molecule/photon)	PTEFs %
[8,14]	2012	Acetone (25–49)	≈44	215–140	3.3–2.2
		Acetaldehyde (160–240)		400–250	5.3–3.3
[12,15]	2016	Acetone (50–250)		50–133	≈10
		Acetaldehyde (65–325)		80–125	≈24

Note: the numbers in parentheses () are the pollutant concentration represented in μmol/L.

5.1. Quantum Yield (QY or φ)

The Quantum Yield is known as an important energy-efficiency estimator used to calculate the photocatalytic photodegradation of organic contaminants (i.e., VOCs). This parameter is commonly based on a number ratio defined as the rate of the photoreaction (photoconverted molecules per unit time) divided by the photon absorption rate (number of photons entering the reactor) [10]. By using this principle, several authors defined Quantum Yields (QYs or φ) as (1) Primary Quantum Yield, (2) Overall Quantum Yield, (3) Apparent or Global Quantum Yield, and (4) Quantum Yield.

Cassano et al. (1995) first defined the concept of Primary Quantum Yield, stating that this efficiency factor must always be smaller than 1. This is considered on the basis that a fraction of photon energy is lost [140].

$$\text{Primary QY} = \frac{\text{moles of pollutant degraded from a primary process/s}}{\text{moles of photons absorbed/s}} \quad (10)$$

Furthermore, Cassano et al. (1995) and Davydov et al. (1999) also proposed and adopted, an Overall Quantum Yield. This parameter, in principle, can be greater than 100%, presenting interesting prospects for photocatalytic processes [141].

$$\text{QY}_{\text{Overall}} = \frac{\text{moles of pollutant degraded via primary and a sec undary process/s}}{\text{moles of photons absorbed/s}} \quad (11)$$

As an alternative, an apparent Quantum Yield (QY_{app}) was considered, using the photons irradiated in a reactor system. This approach, frequently considered in the literature, was a relatively easy one to implement, but much less accurate [16,38,103].

$$\text{QY}_{\text{app}} = \frac{\text{moles of pollutant degraded via a primary process/s}}{\text{moles of photons entering the photoreactor/s}} \quad (12)$$

Salaices et al. (2001) proposed as an option a Quantum Yield defined as the ratio of the $OH^{\bullet}$ radical consumption rate over the absorbed photons rate (P_a). The P_a was initially measured in photocatalytic reactors for pollutant conversion in water by developing macroscopic irradiation energy balances and by accounting for back- and forward-scattering, using spectrophotoradiometers and collimators [53,142]. Later, these measurements were adapted in the Photo-CREC-Air Reactor (PCAR) by Garcia et al. (2010 & 2012), using the ratio of the rate of $OH^{\bullet}$ radicals consumed over the rate of photons absorbed by TiO_2 ($\lambda \leq 388$ nm) [8,14]. The ratio is presented below:

$$\text{QY} = \frac{\text{rate of } OH^{\bullet} \text{ consumed}}{\text{rates of photons absorbed } (P_a)} \quad (13)$$

The rate of $OH^{\bullet}$ radicals consumed can be calculated based on the stoichiometric requirements for the oxidation of the observable chemical species, as is shown in Equation (14). Thus, stoichiometry sets the number of $OH^{\bullet}$ radicals needed at every photocatalytic step as (*j*), in which the lower oxidation species *(i)* ($C_nH_mO_o$) are converted into higher oxidation species as (*h*) ($C_xH_yO_z$). $\nu_{i,j}$ and $\nu_{h,j}$ represent the stoichiometric coefficients for both cases [8,12].

$$\nu_{i,j}C_nH_mO_o + \nu_{OH,j}OH^{\bullet} \rightarrow \nu_{h,j}C_xH_yO_z + \nu_{H_2O,j}H_2O \quad (14)$$

The species involved in the photocatalytic step (*j*) are in agreement with the carbon, hydrogen and oxygen elemental balances. They are represented as

(a) elemental carbon balance:

$$\nu_{i,j}n - \nu_{h,j}x = 0 \quad (15)$$

(b) elemental hydrogen balance:

$$v_{i,j}m + v_{OH,j} - v_{h,j}y - 2v_{H_2O,j} = 0 \quad (16)$$

(c) elemental oxygen balance:

$$v_{i,j}o + v_{OH,j} - v_{h,j}z - v_{H_2O,j} = 0 \quad (17)$$

Therefore, the rate of $OH^{\bullet}$ radical consumption ($Y_{OH^{\bullet},j}$) can be represented as shown below:

$$Y_{OH^{\bullet},T} = \sum Y_{OH^{\bullet},j} = \sum \frac{v_{OH,j}}{v_{i,j}} Y_{i,j} \quad (18)$$

Then, by inserting Equation (18) into Equation (13), one can calculate the Quantum Yield (QY):

$$QY = \frac{-A\sum_1^j Y_{OH^{\bullet},j}}{P_a} = \frac{A\sum_1^j \frac{v_{OH,j}}{v_{i,j}} Y_{i,j}}{P_a} \quad (19)$$

where, $Y_{i,j}$ and $Y_{OH^{\bullet},j}$ are the rate of pollutant degraded molecules "*i*" and the $OH^{\bullet}$ radical consumption (mol/cm^2), respectively; where $v_{i,j}$ stands for the stoichiometric coefficient involved in the photoconversion of species "*i*"; where A is the total area of irradiated photocatalyst, impregnated on the woven SS mesh (cm^2); and where P_a refers as the rate of absorbed photons (mol of photons/s).

In order to assess the P_a, it is important to measure the number of irradiated photons in the PCAR. This is also required in order to be able to design an adequate periscopic probe device (refer to Figure 18). These irradiation measurements begin with an irradiation signal (emitted by P_i) which is received by an optical fiber cable covered by a polished aluminum housing pipe, allowing 90° measurements. This device can be effectively placed at different axial (z), circumferential (θ), and radial positions (r), measuring different wavelengths (λ) and irradiation intensities.

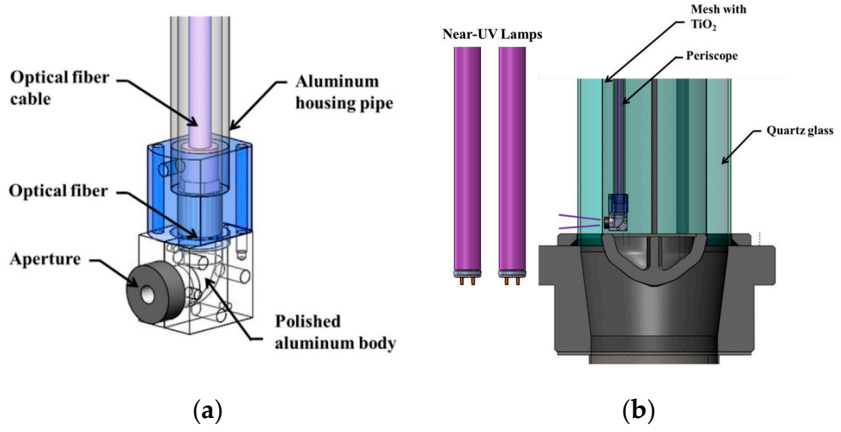

Figure 18. (**a**) Schematic description of the optimal periscopic probe and (**b**) periscope probe orientation in the PCAR. Reproduced by permission of chemical engineering Science [15].

Then, the absorbed photons on the immobilized photocatalyst (P_a) are calculated by implementing a local macroscopic irradiation energy balance:

$$P_a = P_i - P_t - P_r \quad (20)$$

where the incident, transmitted, and reflected photon rates (P_i, P_t, P_r) can be calculated by the following Equation (21); where $q(\theta, z, \lambda)$ represents the radiation measured in (W/cm^2 nm); where λ

stands for the radiation wavelength (nm); where θ and r are the angular and radial positions (° and cm), respectively; and E_{av} denotes the average photon energy (kJ/mol photon).

$$P\ for\ P_i,\ P_t,\ P_r = \frac{r\int_{\lambda_{min}}^{\lambda_{max}}\int_0^{\infty}\int_0^{2\pi} q(\theta,z,\lambda)d\theta dz d\lambda}{E_{av}} \tag{21}$$

Given that only photons with a wavelength (λ_{max}) ≤ than 388 nm activate TiO_2, the average energy (E_{av}) can be estimated as shown below:

$$E_{av} = \frac{\int_{\lambda_{min}}^{\lambda_{max}} q(\theta,z,\lambda)\frac{hc}{\lambda}d\lambda}{\int_{\lambda_{min}}^{\lambda_{max}} q(\theta,z,\lambda)d\lambda} \tag{22}$$

Figure 19a,b show the trajectory of the physically measured photons in the PCAR. Once in contact with the TiO_2 coated SS woven-mesh, the near-UV irradiated photons (P_i) can follow three possible paths: (1) photons can be absorbed (P_a); (2) photons can be reflected (P_r); and (3) photons can be transmitted (P_t).

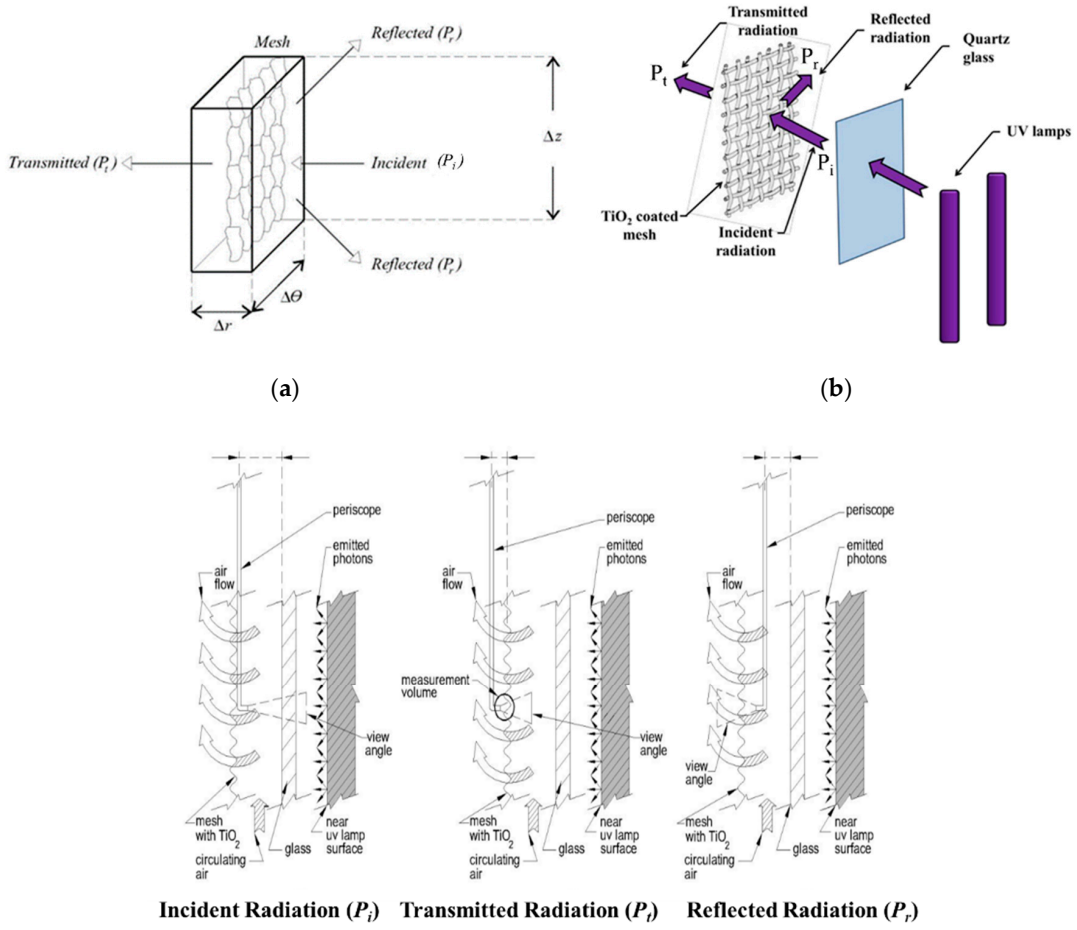

Figure 19. Photo-CREC-Air Reactor: (**a**) schematic diagram of the selected control volume for the macroscopic local radiation energy balance, (**b**) photon trajectory description for near-UV lamps; the photons traverse the quartz glass and reach the woven SS mesh and (**c**) optical probe locations inside the PCAR for radiation measurements. Reproduced with permission of Applied Catalysis B: Environmental [12].

Thus, one can conclude that the ranking of photocatalytic reactor designs requires the use of the more mechanistically sound QYs, as considered by Equation (13). This can be achieved: (a) by detecting measurable organic species (model pollutants, intermediates) and their changes at every step of the photoconversion, which is relevant to establishing the $OH^{\bullet}$ consumption rates via stoichiometric relations; and (b) by calculating absorbed photon rates using macroscopic irradiation energy balances.

5.2. Photochemical Thermodynamic Efficiency Factors (PTEFs)

In 1997, Serrano and de Lasa (1997) introduced the PTEF to establish photocatalytic reactor efficiencies using thermodynamic principles. While the PTEF was originally considered for the photodegradation of organic pollutants in water [143], Garcia et al. (2010) and Lugo et al. (2016) later extended the PTEF to the photoconversion of airborne pollutants [14,15]. Furthermore, this concept was further developed by Escobedo et al. (2019), who applied the PTEF to photocatalytic hydrogen production [44].

Regarding the PTEF, one can consider an overall energy balance as shown below:

$$Q_{abs} - Q_{loss} - Q_{used} = \frac{dE}{dt} \tag{23}$$

where, *dE/dt* denotes the energy accumulation in the system; where Q_{abs} is the absorbed radiation energy on the photocatalyst; where Q_{loss} accounts for the energy released as heat; and where Q_{used} stands for the $OH^{\bullet}$ radical energy formation used for VOCs mineralization. Q variables are expressed in *J/min* units.

If one disregards the *dE/dt* energy accumulation, which is an adequate approximation in photocatalytic reactors operating isothermally Serrano et al. (1997) [143] and Lugo-Vega et al. (2016) [15], then Equation (24), can be simplified as $Q_{abs} - Q_{loss} - Q_{used} = 0$ [15]; with Q_{used} and Q_{abs} being used to calculate the PTEF energy efficiency as shown below:

$$PTEF = \frac{Q_{used}}{Q_{abs}} \tag{24}$$

Thus, the PTEF is also equal to the enthalpy invested in the formation of the $OH^{\bullet}$ radicals ($\Delta H_{OH^{\bullet}}$) in (J/mol) over the energy content of the absorbed photons. It can be alternatively expressed as:

$$PTEF = \frac{-AY_{OH^{\bullet}} \Delta H_{OH^{\bullet}}}{Q_{abs}} = \mathrm{QY} * n_{OH^{\bullet}} \tag{25}$$

where, $n_{OH^{\bullet}}$ stands for the fraction of photon energy used to form $OH^{\bullet}$ radicals as shown below:

$$n_{OH^{\bullet}} = \frac{\Delta H_{OH^{\bullet}}}{E_{av}} \tag{26}$$

One should note that the enthalpy of formation assignments to $OH^{\bullet}$ radicals is an evaluation that has to be carefully developed, as reported by CREC-UWO researchers [15,143].

Table 5 reports both the percentual Quantum Yields (QYs%) and the PTEFs%. One should note that the QYs% reported in Table 5 are limited to those involving meaningful $OH^{\bullet}$ radical consumption and photon absorbed ratios. Similarly, the PTEFs% reported consider energy ratios involving the energy content of the $OH^{\bullet}$ radicals consumed over the energy content of the photons absorbed.

It interesting to note, as reported in Table 5, that QY% in the Photo-CREC-Air are in excess of 100%. This confirms (a) the excellent design of Photo-CREC-Air units, and (b) the applicability of the postulated photocatalytic reaction mechanism, with 3 near-UV photons yielding 4 $OH^{\bullet}$ groups, corresponding to a theoretical Quantum Yield of 133% [8,15,16,38].

6. Challenges and Opportunities for Photocatalytic Conversion of Air Pollutants

Photo-CREC-Air units with high QYs display performances that agree with the high anticipated QYs via mechanistic formulations. Despite this, the application of high QYs in photocatalysis, for the removal of VOCs, is limited to modest air volumes, such as the ones in paint shops or enclosed office spaces in buildings. In fact, the engineering of near-UV powered photocatalytic reactors for larger air volumes such as open-concept office spaces still presents challenges. One could argue that while there may be renewed opportunities for visible light irradiated photocatalysts for VOCs conversion [144–149], applications of these photocatalysts would likely be limited to small air volume purification.

The recent outbreak of the SARS-CoV2 (COVID-19) virus offers, however, new opportunities for photocatalytic reactors, which could be engineered using the Photo-CREC-Air principles discussed in the present review. A possible significant application of the Photo-CREC-Air Reactor today is for hospitals. The Photo-CREC-Air could help provide safe enclosed spaces with adequate patient isolation and the protection of the medical personnel. By helping keep enclosed hospital spaces "uncontaminated" from COVID-19, the Photo-CREC-Air Reactor could prevent virus outbreaks in other hospital areas. Another possible scenario is in dental clinics, where keeping enclosed spaces uncontaminated is now a requirement. Therefore, there is a need for new technologies for the photo-inactivation of the COVID-19 virus "on-site".

Currently, the most popular approaches for the inactivation of viruses consider the use of UVC (Ultraviolet-C, 254 nm) germicidal lamps. While UVC germicidal lamps are very effective, their application requires the personnel who operate them to be very experienced. This is the case given the safety-related issues with UVC usage, such as skin cancer and photokeratitis (cornea inflammation) [150–152]. On the other hand, there is another claimed alternative for the inactivation of viruses developed by air ventilation equipment manufacturers. This option uses HEPA filters in an air ventilation apparatus [153–155]. While a HEPA filter has the capability of trapping 0.12-micron SARS-CoV2 particles, it does not inactivate SARS-CoV2 (COVID-19). As a result, this creates a potential health issue with filter disposal [156].

Thus, the current circumstances of the SARS-CoV2 (COVID-19) pandemic open new opportunities for the development of new photocatalytic air treatment units, adapted from a Photo-CREC-Air Reactor using lower energetic near-UV photons and a TiO_2 photocatalyst. These photocatalytic systems could inactivate the COVID-19 virus, as well as other viruses, while being much more operationally safe. These units could be run by non-specialized personnel, and thus, be a valuable solution in hospitals, dental clinics, restaurants, classrooms, and many other enclosed areas.

The re-engineering of the Photo-CREC-Air Reactor for COVID-19 virus inactivation could consist of the re-design of irradiated mesh surfaces with photocatalysts supported on them, via strong particle-surface forces. This would secure COVID-19 virus capture and inactivation at irradiated locations. One should note that the comprehensive demonstration of the new Photo-CREC-Air Reactor high performance for the inactivation of viruses could involve using viruses that are non-pathogenic to humans such as MS2.

Also, de Lasa et al. (2005) proposed an Inactivation Quantum Yields *(IQY)* parameter, accounting for the ratio of the number of carbon atoms inactivated over the number of photons absorbed as shown below [10]:

$$IQY = \frac{\left[\frac{dN_C}{dt}\right]_{in}}{P_a} = \frac{(moles\ of\ Organic\ Carbon\ Inactivated/s)}{(moles\ of\ photonos\ absorbed/s)} \quad (27)$$

Stuart et al. (2003) developed and established *IQY* experiments in a 6 L Photo-CREC Water-II reactor with 0.24 g of Degussa P25 TiO_2/L and powered with a 15 W near-UV lamp [157]. The inactivation of both MS2 bacteriophage (ATCC-15597-B1) and *E. coli* were considered. One should note that monitoring the MS2 failure to infect the *E. coli* allowed one to assess the progress of MS2 inactivation [157,158]. Virus particles from bacterial lysates were purified, concentrated, and titrated to determine the number of PFU (particle forming units) per milliliter. Nonlinear regression was used to determine the

inactivation kinetics of MS2 and *E. coli*. It was observed that TiO_2-based photocatalysis showed good MS2 inactivation, with no virus inactivation under control conditions: (a) near-UV light only and (b) photocatalyst only. Furthermore, *E. coli* inactivation also occurred in each of the controls, with *E. coli* survival being likely affected by shear from the pump.

Table 6 reports IQYs% for a concentration of 1×10^4 particles (or cells) per milliliter. In both cases, and despite the observed differences, IQYs% for MS2 were 2200%.

Table 6. IQYs% for *E. coli* and MS2 bacteriophage using TiO_2-near UV-mediated inactivation [10,157].

Organism	First Order Inactivation Constant (min^{-1})	IQYs% (Carbons Inactivated/Photon)
MS2 Bacteriophage	0.8175	2200
E. coli	0.2377	5.19×10^7

Note: Average carbon content in MS2 and *E. coli* assessed at 1.16×10^5 and 7.27×10^9, respectively.

Regarding the IQYs% for both MS2 and *E.coli*, reported values are very encouraging. These very high IQYs% point to the MS2 inactivation mechanism, where one near-UV photon can turn an MS2 bacteriophage structure containing a large number of carbons (e.g., 1.16×10^5) into a non-viable one.

Furthermore, and on this basis, it is also anticipated that virus inactivation with very high IQYs could be accomplished in photocatalytic units for air treatment. Thus, it is anticipated that today that Photo-CREC-Air units could provide a unique solution for the inactivation of SARS-CoV2 (COVID-19) viruses in enclosed hospital spaces.

7. Conclusions

(a) TiO_2-based photocatalysts irradiated with near-UV light offer an important application for the photocatalytic oxidation of organic pollutants (i.e., VOCs), both in air and water.

(b) TiO_2 photocatalysts are exceptional materials for the photoconversion of organic pollutants. These semiconductor materials can be modified by a diversity of methods such as deposition, impregnation, or doping.

(c) A diversity of immobilization techniques can be employed for PCO. The immobilization selection method is dependent on the mesh material type (i.e., quartz, glass, stainless steel, polymers, or fabric).

(d) CFD models allow the effective pretesting of various operational conditions and flow patterns in photocatalytic reactors.

(e) Different reaction mechanisms can be considered for the complete mineralization of VOCs into CO_2 and H_2O, with the "parallel-in series" method proving to be a most relevant approach for the photoconversion of organic pollutants in air and water.

(f) Macroscopic irradiation energy balances are required to calculate the photons absorbed by the semiconductor material during PCO.

(g) Tracking all chemical species, including model pollutants and intermediates, is required to assess $OH^{\bullet}$ consumption rates.

(h) Quantum Yields provide energy efficiencies in photocatalytic reactors, with an adequate definition based on the ratio of $OH^{\bullet}$ radicals consumed over the rate of photons absorbed by the photocatalyst.

(i) The PTEF is a valuable parameter to determine photocatalytic reactor efficiencies on the basis of thermodynamics principles.

(j) Photocatalytic reactors have the potential to be re-engineered for SARS-CoV2 (COVID-19) virus inactivation in hospitals and other indoor enclosed spaces. It is anticipated that this will be achieved with high *IQYs* (Inactivation Quantum Yields).

Author Contributions: Investigation, preparation and writing of the original-draft review article, S.E.; writing, review and editing of the manuscript, H.d.L. All authors have read and agreed to the published version of the manuscript.

Funding: This research was funded by Western University and the Natural Science and Engineering Research Council of Canada (NSERC), through grants awarded to Hugo de Lasa.

Acknowledgments: The authors would like to thank Florencia de Lasa, who assisted with the editing and proofreading of this manuscript.

Conflicts of Interest: The authors declare no conflict of interest.

Nomenclature

A	Uniformly irradiated mesh area holding an optimum loading of TiO_2 (m^2)
Ag	Silver
Au	Gold
c	Speed of light (3×10^8 m/s)
C	Carbon
$Co(CH_3CO_2)_2$	Cobalt (II) acetate
C_2H_4O	Acetaldehyde
C_3H_6O	Acetone
$Mn(CH_3CO_2)_2$	Manganese (II) acetate
CO_2	Carbon dioxide
Co	Cobalt
Cr	Chrome
C_{Ac}	Acetone concentration (kg/m^3)
$C_{eq,i}$	Equilibrium of species "i" in the gas phase concentration (mol/m^3 or ppm)
$C_{eq,Inf}$	Inflection point observed on the adsorption isotherm (mol/m^3)
D	Diffusivity of acetone in air (m^2/s)
$D_{p\text{-}BJH}$	Pore diameter (nm)
D_t	Eddy diffusivity (m^2/s)
e^-	Electron
E_{av}	Average photon energy (kJ/mol photon).
E_{BG}	Energy band gap (eV)
eV	Electron volts
Fe	Iron
Fe^{+3}	Iron-III
h	Planck's constant (6.63×10^{-34} J/s))
h^+	Hole
H_2O	Water
HNO_3	Nitric acid
K	Permeability (m^2)
k_i	Equilibrium kinetic constant of specie "i" ($mol/s\ m^3$)
$K^A_{eq,i}$	Adsorption equilibrium constant (m^3/mol or ppm^{-1})
$K^{A1}_{eq,i}$	Langmuir adsorption equilibrium constant (m^3/mol or ppm^{-1})
$K^{A2}_{eq,i}$	Freundlich adsorption equilibrium constant (m^3/mol or ppm^{-1})
L	Liters
Mn	Manganese
MS2	Non-pathogenicity to humans norovirus structure
n	Number of layers
N	Nitrogen (solid)
N_2	Nitrogen (gas)
NH_3	Ammonia
NH_4F	Ammonium fluoride
NH_4VO_3	Ammonium metavanadate

NO	Nitrogen oxide
NO_2	Nitrogen dioxide
$[N_C]_{in}$	Carbon atoms at initial conditions (atoms of carbon inactivated/s)
O^-	Oxidized
O_2	Oxygen
O_2^-	Superoxide radicals
$OH^\bullet$	Hydroxyl radicals
P_a	Rate of absorbed photons (mol of photons/s).
P_i	Incident radiation
P_r	Reflected radiation
P_t	Transmitted radiation
Pd	Palladium
Pt	Platinum
$q\ (\theta,z,\lambda)$	Radiation measured (W/cm^2 nm)
$Q_{eq,\ ads}$	Existing equilibrium adsorption surface concentration (mol/g_{cat})
$Q_{eq,\ max}$	Maximum equilibrium adsorption surface concentration (mol/g_{cat})
$Q_{eq,\ max\text{-}1}$	Langmuir maximum equilibrium adsorption surface concentrations (mol/g_{cat})
$Q_{eq,\ max\text{-}2}$	Freundlich maximum equilibrium adsorption surface concentrations (mol/g_{cat})
R^+	Reduced
S	Sulphur
S_{BET}	Surface Area (m^2/g)
S_C	Acetone source/sink term (kg/m^3 s)
S_M	Momentum source/sink term (kg/m^2 s^2)
t	Time (s)
Ti	Titanium
$TiCl_4$	Titanium tetrachloride
TiO_2	Titanium dioxide
$Ti(OCH(CH_3)_2)_4$	Titanium tetraisopropoxide
V	Total volume in PCAR reactors (m^3)
V	Vanadium
V_2O_5	Vanadium (V) oxide
$V_{p\text{-}BJH}$	Pore volume (cm^3/g)
$W(CO_6)$	Tungsten hexacarbonyle
wt.%	Weight percent (%)
Acronyms	
A	Anatase
AAS-ASC	Air Assisted Spray-Automatized Spinning Coating
BET	Brunauer-Emmett-Teller
BJH	Barrett-Joyner-Halenda
BTX	Benzene-Toluene-Xylene
CB	Conduction Band
CFD	Computational Fluid Dynamics
COVID-19	Corona Virus -19 (SARS-CoV2)
CREC	Chemical Reactor Engineer Centre
CVD	Chemical Vapor Deposition
DB	Debye Sherrer
DP25	Degussa P25 (Commercial TiO_2)
FQE	Formal Quantum Efficiency
HEPA	High-Efficiency Particulate Air Filter
IQYs	Inactivation Quantum Yields
LED	Light-Emitting Diode
LH	Langmuir-Hinshelwood
MIEB	Macroscopic Irradiation Energy Balances
PAHs	Polycyclic Aromatic Hydrocarbons
PCAR	Photocatalytic Oxidation

PFU	Particle Forming Units
PTEFs	Photocatalytic Thermodynamic Efficiency Factors
PU	Porous Polyurethane
QYs	Quantum Yields
QY_{app}	Apparent Quantum Yield
R	Rutile
RVE	Representative Volume Element
SARS	Severe Acute Respiratory Syndrome
SS	Stainless Steel
SST	Shear Stress Transport
UV	Ultraviolet
VB	Valence Band
VOCs	Volatile Organic Compounds
VUV	Vacuum Ultraviolet
Symbols	
θ	Angular position (°)
θ_A	Dimensionless surface species concentration
r_i	Rate of photoconversion of the model pollutant "i" (mol/min*m^2)
$\Delta H_{OH\bullet}$	Enthalpy invested in the formation of the $OH^\bullet$ radicals (J/mol)
λ	Radiation wavelength (nm)
ρ	Fluid density (kg/m^3)
U	Fluid velocity vector (m/s)
U_S/U_{Max}	Dimensionless ratio between the interface slip velocity
τ	Stress tensor (N/m^2)
τ_t	Reynolds stress tensor (N/m^2)
ν	Stoichiometric coefficient
r	Radial position (cm)
$n_{OH\bullet}$	Fraction of photon energy used to form $OH^\bullet$ radicals
∇	Gradient vector of x, y and z coordinates
$\otimes$	Tensor product

References

1. Nakano, R.; Ishiguro, H.; Yao, Y.; Kajioka, J.; Fujishima, A.; Sunada, K.; Minoshima, M.; Hashimoto, K.; Kubota, Y. Photocatalytic inactivation of influenza virus by titanium dioxide thin film. *Photochem. Photobiol. Sci.* **2012**, *11*, 1293–1298. [CrossRef]
2. Ibrahim, H.; Lasa, H. de Photo-catalytic conversion of air borne pollutants Effect of catalyst type and catalyst loading in a novel photo-CREC-air unit. *Appl. Catal. B Environ.* **2002**, *38*, 201–213. [CrossRef]
3. Lugo-Vega, C.S. Evaluation of VOC Degradation in Photo- Catalytic Air Reactors: TiO_2 Immobilization, Energy Efficiency and Kinetic Modeling. Ph.D. Thesis, University of Western Ontario, London, ON, Canada, 2016.
4. Hakim, M.; Broza, Y.Y.; Barash, O.; Peled, N.; Phillips, M.; Amann, A.; Haick, H. Volatile organic compounds of lung cancer and possible biochemical pathways. *Chem. Rev.* **2012**, *112*, 5949–5966. [CrossRef]
5. Dales, R.; Liu, L.; Wheeler, A.J.; Gilbert, N.L. Quality of indoor residential air and health. *Can. Med. Assoc. J.* **2008**, *179*, 147–152. [CrossRef]
6. Indoor Air Quality | EPA's Report on the Environment (ROE) | US EPA. Available online: https://www.epa.gov/report-environment/indoor-air-quality (accessed on 20 April 2020).
7. Klepeis, N.E.; Nelson, W.C.; Ott, W.R.; Robinson, J.P.; Tsang, A.M.; Switzer, P.; Behar, J.V.; Hern, S.C.; Engelmann, W.H. The National Human Activity Pattern Survey (NHAPS): A resource for assessing exposure to environmental pollutants. *J. Expo. Anal. Environ. Epidemiol.* **2001**, *11*, 231–252. [CrossRef] [PubMed]
8. Garcia-Hernandez, J.M.; Serrano-Rosales, B.; De Lasa, H. Energy efficiencies in a photo-CREC-air reactor: Conversion of model organic pollutants in air. *Ind. Eng. Chem. Res.* **2012**, *51*, 5715–5727. [CrossRef]
9. Castrillón, S.R.V.; De Lasa, H.I. Performance evaluation of photocatalytic reactors for air purification using Computational Fluid Dynamics (CFD). *Ind. Eng. Chem. Res.* **2007**, *46*, 5867–5880. [CrossRef]

10. De Lasa, H.; Serrano, B.; Salaices, M. *Photocatalytic Reaction Engineering*, 1st ed.; Springer: Berlin/Heidelberg, Germany, 2005; ISBN 978-0-387-27591-8.
11. Sirivallop, A.; Areerob, T.; Chiarakorn, S. Enhanced Visible Light Photocatalytic Activity of N and Ag Doped and Co-Doped TiO_2 Synthesized by Using an In-Sity Solvothermal Method for Gas Phase Ammonia Removal. *Catalysts* **2020**, *10*, 251. [CrossRef]
12. Lugo-Vega, C.S.; Serrano-Rosales, B.; de Lasa, H. Immobilized particle coating for optimum photon and TiO_2 utilization in scaled air treatment photo reactors. *Appl. Catal. B Environ.* **2016**, *198*, 211–223. [CrossRef]
13. Romero-Vargas Castrillón, S.; Ibrahim, H.; De Lasa, H. Flow field investigation in a photocatalytic reactor for air treatment (Photo-CREC-air). *Chem. Eng. Sci.* **2006**, *61*, 3343–3361. [CrossRef]
14. Hernandez, J.M.G.; Rosales, B.S.; de Lasa, H. The photochemical thermodynamic efficiency factor (PTEF) in photocatalytic reactors for air treatment. *Chem. Eng. J.* **2010**, *165*, 891–901. [CrossRef]
15. Lugo-Vega, C.S.; Serrano-Rosales, B.; de Lasa, H. Energy efficiency limits in Photo-CREC-Air photocatalytic reactors. *Chem. Eng. Sci.* **2016**, *156*, 77–88. [CrossRef]
16. Ibrahim, H.; de Lasa, H. Photo-catalytic degradation of air borne pollutants apparent quantum efficiencies in a novel photo-CREC-air reactor. *Chem. Eng. Sci.* **2003**, *58*, 943–949. [CrossRef]
17. Rusinque, B.; Escobedo, S.; de Lasa, H. Photocatalytic Hydrogen Production Under Near-UV Using Pd-Doped Mesoporous TiO_2 and Ethanol as Organic Scavenger. *Catalysts* **2019**, *9*, 33. [CrossRef]
18. Escobedo, S.; Serrano, B.; de Lasa, H. Quantum yield with platinum modified TiO_2 photocatalyst for hydrogen production. *Appl. Catal. B Environ.* **2013**, 523–536. [CrossRef]
19. Rusinque, B.; Escobedo, S.; de Lasa, H. Photoreduction of a Pd-Doped Mesoporous TiO_2 Photocatalyst for Hydrogen Production under Visible Light. *Catalysts* **2020**, *10*, 74. [CrossRef]
20. Deng, X.; Yue, Y.; Gao, Z. Gas-phase photo-oxidation of organic compounds over nanosized TiO_2 photocatalysts by various preparations. *Appl. Catal. B Environ.* **2002**, *39*, 135–147. [CrossRef]
21. Benmami, M.; Chhor, K.; Kanaev, A.V. High photocatalytic activity of monolayer nanocoatings prepared from non-crystalline titanium oxide sol nanoparticles. *Chem. Phys. Lett.* **2006**, *422*, 552–557. [CrossRef]
22. Esterkin, C.R.; Negro, A.C.; Alfano, O.M.; Cassano, A.E. Air pollution remediation in a fixed bed photocatalytic reactor coated with TiO_2. *AIChE J.* **2003**, *51*, 2298–2310. [CrossRef]
23. Peill, N.J.; Hoffmann, M.R. Development and Optimization of a TiO_2-Coated Fiber-Optic Cable Reactor: Photocatalytic Degradation of 4-Chlorophenol. *Environ. Sci. Technol.* **1995**, *29*, 2974–2981. [CrossRef]
24. Zhu, R.; Che, S.; Liu, X.; Lin, S.; Xu, G.; Ouyang, F. A novel fluidized-bed-optical-fibers photocatalytic reactor (FBOFPR) and its performance. *Appl. Catal. A Gen.* **2014**, *471*, 136–141. [CrossRef]
25. Wu, Y.T.; Yu, Y.H.; Nguyen, V.H.; Lu, K.T.; Wu, J.C.S.; Chang, L.M.; Kuo, C.W. Enhanced xylene removal by photocatalytic oxidation using fiber-illuminated honeycomb reactor at ppb level. *J. Hazard. Mater.* **2013**, *262*, 717–725. [CrossRef] [PubMed]
26. Du, P.; Carneiro, J.T.; Moulijn, J.A.; Mul, G. A novel photocatalytic monolith reactor for multiphase heterogeneous photocatalysis. *Appl. Catal. A Gen.* **2008**, *334*, 119–128. [CrossRef]
27. Monteiro, R.A.R.; Miranda, S.M.; Rodrigues-Silva, C.; Faria, J.L.; Silva, A.M.T.; Boaventura, R.A.R.; Vilar, V.J.P. Gas phase oxidation of n-decane and PCE by photocatalysis using an annular photoreactor packed with a monolithic catalytic bed coated with P25 and PC500. *Appl. Catal. B Environ.* **2015**, *165*, 306–315. [CrossRef]
28. Han, Z.; Chang, V.W.C.; Zhang, L.; Tse, M.S.; Tan, O.K.; Hildemann, L.M. Preparation of TiO_2-coated polyester fiber filter by spray-coating and its photocatalytic degradation of gaseous formaldehyde. *Aerosol Air Qual. Res.* **2012**, *12*, 1327–1335. [CrossRef]
29. Birnie, M.; Riffat, S.; Gillott, M. Photocatalytic reactors: Design for effective air purification. *Int. J. Low-Carbon Technol.* **2006**, *1*, 47–58. [CrossRef]
30. Hou, W.M.; Ku, Y. Photocatalytic decomposition of gaseous isopropanol in a tubular optical fiber reactor under periodic UV-LED illumination. *J. Mol. Catal. A Chem.* **2013**, *374–375*, 7–11. [CrossRef]
31. Ibrahim, H.; De Lasa, H. Kinetic Modeling of the Photocatalytic Degradation of Air-Borne Pollutants. *AIChE J.* **2004**, *50*, 1017–1027. [CrossRef]
32. Kočí, K.; Reli, M.; Kozák, O.; Lacný, Z.; Plachá, D.; Praus, P.; Obalová, L. Influence of reactor geometry on the yield of CO_2 photocatalytic reduction. *Catal. Today* **2011**, *176*, 212–214. [CrossRef]
33. Lugo-Vega, C.S.; Moreira, J.; Serrano-Rosales, B.; de Lasa, H. Kinetics of the pollutant photocatalytic conversion in a Photo-CREC-Air Reactor. *Chem. Eng. J.* **2017**, *317*, 1069–1082. [CrossRef]

34. Escobedo, S.; Serrano, B.; Calzada, A.; Moreira, J.; de Lasa, H. Hydrogen production using a platinum modified TiO_2 photocatalyst and an organic scavenger. Kinetic modeling. *Fuel* **2016**, *181*, 438–449. [CrossRef]
35. Vincent, G.; Schaer, E.; Marquaire, P.M.; Zahraa, O. CFD modelling of an annular reactor, application to the photocatalytic degradation of acetone. *Process Saf. Environ. Prot.* **2011**, *89*, 35–40. [CrossRef]
36. Boyjoo, Y.; Ang, M.; Pareek, V. Some aspects of photocatalytic reactor modeling using computational fluid dynamics. *Chem. Eng. Sci.* **2013**, *101*, 764–784. [CrossRef]
37. Queffeulou, A.; Geron, L.; Schaer, E. Prediction of photocatalytic air purifier apparatus performances with a CFD approach using experimentally determined kinetic parameters. *Chem. Eng. Sci.* **2010**, *65*, 5067–5074. [CrossRef]
38. Ibrahim, H.; De Lasa, H. Novel photocatalytic reactor for the destruction of airborne pollutants reaction kinetics and quantum yields. *Ind. Eng. Chem. Res.* **1999**, *38*, 3211–3217. [CrossRef]
39. Garcia-Segura, S.; Dosta, S.; Guilemany, J.M.; Brillas, E. Solar photoelectrocatalytic degradation of Acid Orange 7 azo dye using a highly stable TiO_2 photoanode synthesized by atmospheric plasma spray. *Appl. Catal. B Environ.* **2013**, *132–133*, 142–150. [CrossRef]
40. Houas, A.; Lachheb, H.; Ksibi, M.; Elaloui, E.; Guillard, C.; Herrmann, J.M. Photocatalytic degradation pathway of methylene blue in water. *Appl. Catal. B Environ.* **2001**, *31*, 145–157. [CrossRef]
41. Zhao, J.; Chen, C.; Ma, W. Photocatalytic Degradation of Organic Pollutants Under Visible Light Irradiation. *Top. Catal.* **2005**, *35*, 269–278. [CrossRef]
42. Kudo, A.; Miseki, Y. Heterogeneous photocatalyst materials for water splitting. *Chem. Soc. Rev.* **2009**, *38*, 253–278. [CrossRef]
43. Serrano, B.; Ortíz, A.; Moreira, J.; De Lasa, H.I. Energy efficiency in photocatalytic reactors for the full span of reaction times. *Ind. Eng. Chem. Res.* **2009**, *48*, 9864–9876. [CrossRef]
44. Escobedo, S.; Rusinque, B.; de Lasa, H. Photochemical Thermodynamic Efficiency Factors (PTEFs) for Hydrogen Production Using Different TiO_2 Photocatalysts. *Ind. Eng. Chem. Res.* **2019**, *58*, 22225–22235. [CrossRef]
45. Serrano, B.; Ortíz, A.; Moreira, J.; De Lasa, H.I. Photocatalytic thermodynamic efficiency factors. Practical limits in photocatalytic reactors. *Ind. Eng. Chem. Res.* **2010**, *49*, 6824–6833. [CrossRef]
46. Keller, V.; Keller, N.; Ledoux, M.J.; Lett, M.C. Biological agent inactivation in a flowing air stream by photocatalysis. *Chem. Commun.* **2005**, 2918–2920. [CrossRef]
47. Gerrity, D.; Ryu, H.; Crittenden, J.; Abbaszadegan, M. Photocatalytic inactivation of viruses using titanium dioxide nanoparticles and low-pressure UV light. *J. Environ. Sci. Heal.—Part A Toxic/Hazardous Subst. Environ. Eng.* **2008**, *43*, 1261–1270. [CrossRef] [PubMed]
48. Kim, J.; Jang, J. Inactivation of airborne viruses using vacuum ultraviolet photocatalysis for a flow-through indoor air purifier with short irradiation time. *Aerosol Sci. Technol.* **2018**, *52*, 557–566. [CrossRef]
49. Yao, Y.; Ochiai, T.; Ishiguro, H.; Nakano, R.; Kubota, Y. Antibacterial performance of a novel photocatalytic-coated cordierite foam for use in air cleaners. *Appl. Catal. B Environ.* **2011**, *106*, 592–599. [CrossRef] [PubMed]
50. Bedia, J.; Muelas-Ramos, V.; Peñas-Garzón, M.; Gómez-Avilés, A.; Rodríguez, J.J.; Belver, C. A review on the synthesis and characterization of metal organic frameworks for photocatalytic water purification. *Catalysts* **2019**, *9*, 52. [CrossRef]
51. Fujishima, A.; Zhang, X. Titanium dioxide photocatalysis: Present situation and future approaches. *Comptes Rendus Chim.* **2006**, *9*, 750–760. [CrossRef]
52. Ismail, A.A.; Bahnemann, D.W. Mesoporous titania photocatalysts: Preparation, characterization and reaction mechanisms. *J. Mater. Chem.* **2011**, *21*, 11686–11707. [CrossRef]
53. Salaices, M.; Serrano, B.; De Lasa, H.I. Photocatalytic conversion of organic pollutants extinction coefficients and quantum efficiencies. *Ind. Eng. Chem. Res.* **2001**, *40*, 5455–5464. [CrossRef]
54. Rosales, B.S.; Moreira Del Rio, J.; Guayaquil, J.F.; De Lasa, H. Photodegradation Efficiencies in a Photo-CREC Water-II Reactor Using Several TiO_2 Based Catalysts. *Int. J. Chem. React. Eng.* **2016**, *14*, 685–701. [CrossRef]
55. Bianchi, C.L.; Gatto, S.; Pirola, C.; Naldoni, A.; Di Michele, A.; Cerrato, G.; Crocellà, V.; Capucci, V. Photocatalytic degradation of acetone, acetaldehyde and toluene in gas-phase: Comparison between nano and micro-sized TiO_2. *Appl. Catal. B Environ.* **2014**, *146*, 123–130. [CrossRef]

56. Haghighatmamaghani, A.; Haghighat, F.; Lee, C.S. Performance of various commercial TiO_2 in photocatalytic degradation of a mixture of indoor air pollutants: Effect of photocatalyst and operating parameters. *Sci. Technol. Built Environ.* **2019**, *25*, 600–614. [CrossRef]
57. Nuño, M.; Ball, R.J.; Bowen, C.R. Photocatalytic Properties of Commercially Available TiO_2 Powders for Pollution Control. In *Semiconductor Photocatalysis—Materials, Mechanisms and Applications*; InTech: Vienna, Austria, 2016. [CrossRef]
58. Sun, H.; Ullah, R.; Chong, S.; Ang, H.M.; Tadé, M.O.; Wang, S. Room-light-induced indoor air purification using an efficient Pt/N-TiO_2 photocatalyst. *Appl. Catal. B Environ.* **2011**, *108–109*, 127–133. [CrossRef]
59. Christoforidis, K.C.; Figueroa, S.J.A.; Fernández-García, M. Iron-sulfur codoped TiO_2 anatase nano-materials: UV and sunlight activity for toluene degradation. *Appl. Catal. B Environ.* **2012**, *117–118*, 310–316. [CrossRef]
60. Pham, T.D.; Lee, B.K. Novel adsorption and photocatalytic oxidation for removal of gaseous toluene by V-doped TiO_2/PU under visible light. *J. Hazard. Mater.* **2015**, *300*, 493–503. [CrossRef]
61. Gurulakshmi, M.; Selvaraj, M.; Selvamani, A.; Vijayan, P.; Sasi Rekha, N.R.; Shanthi, K. Enhanced visible-light photocatalytic activity of V_2O_5/S-TiO_2 nanocomposites. *Appl. Catal. A Gen.* **2012**, *449*, 31–46. [CrossRef]
62. Almomani, F.; Bhosale, R.; Shawaqfah, M. Solar oxidation of toluene over Co doped nano-catalyst. *Chemosphere* **2020**, *255*, 126878. [CrossRef]
63. Huang, H.; Huang, H.; Zhang, L.; Hu, P.; Ye, X.; Leung, D.Y.C. Enhanced degradation of gaseous benzene under vacuum ultraviolet (VUV) irradiation over TiO2 modified by transition metals. *Chem. Eng. J.* **2015**, *259*, 534–541. [CrossRef]
64. Zhu, S.; Wang, D. Photocatalysis: Basic principles, diverse forms of implementations and emerging scientific opportunities. *Adv. Energy Mater.* **2017**, *7*, 1–24. [CrossRef]
65. Liu, L.; Li, Y. Understanding the reaction mechanism of photocatalytic reduction of CO_2 with H_2O on TiO_2-based photocatalysts: A review. *Aerosol Air Qual. Res.* **2014**, *14*, 453–469. [CrossRef]
66. Ajmal, A.; Majeed, I.; Malik, R.N.; Idriss, H.; Nadeem, M.A. Principles and mechanisms of photocatalytic dye degradation on TiO_2 based photocatalysts: A comparative overview. *RSC Adv.* **2014**, *4*, 37003–37026. [CrossRef]
67. Hirakawa, T.; Koga, C.; Negishi, N.; Takeuchi, K.; Matsuzawa, S. An approach to elucidating photocatalytic reaction mechanisms by monitoring dissolved oxygen: Effect of H_2O_2 on photocatalysis. *Appl. Catal. B Environ.* **2009**, *87*, 46–55. [CrossRef]
68. Yang, Y.; Zhong, H.; Tian, C. Photocatalytic mechanisms of modified titania under visible light. *Res. Chem. Intermed.* **2011**, *37*, 91–102. [CrossRef]
69. Wang, K.; Tsai, H.; Hsieh, Y. A study of photocatalytic degradation of trichloroethylene in vapor phase on TiO_2 photocatalyst. *Chemosphere* **1998**, *36*, 2763–2773. [CrossRef]
70. Barakat, C.; Gravejat, P.; Guaitella, O.; Thevenet, F.; Rousseau, A. Oxidation of isopropanol and acetone adsorbed on TiO_2 under plasma generated ozone flow: Gas phase and adsorbed species monitoring. *Appl. Catal. B Environ.* **2014**, *147*, 302–313. [CrossRef]
71. Kim, M.S.; Liu, G.; Nam, W.K.; Kim, B.W. Preparation of porous carbon-doped TiO_2 film by sol-gel method and its application for the removal of gaseous toluene in the optical fiber reactor. *J. Ind. Eng. Chem.* **2011**, *17*, 223–228. [CrossRef]
72. Yang, G.; Jiang, Z.; Shi, H.; Xiao, T.; Yan, Z. Preparation of highly visible-light active N-doped TiO_2 photocatalyst. *J. Mater. Chem.* **2010**, *20*, 5301–5309. [CrossRef]
73. Li, D.; Haneda, H.; Hishita, S.; Ohashi, N. Visible-light-driven N-F-codoped TiO_2 photocatalysts. 1. Synthesis by spray pyrolysis and surface characterization. *Chem. Mater.* **2005**, *17*, 2588–2595. [CrossRef]
74. Salas, S.E.; Hugo De Lasa, S. Photocatalytic Water Splitting using a Modified Pt- TiO_2. Kinetic Modeling and Hydrogen Production Efficiency. Ph.D. Thesis, University of Western Ontario, London, ON, Canada, 2013.
75. Imoberdorf, G.E.; Irazoqui, H.A.; Alfano, O.M.; Cassano, A.E. Scaling-up from first principles of a photocatalytic reactor for air pollution remediation. *Chem. Eng. Sci.* **2007**, *62*, 793–804. [CrossRef]
76. Arsac, F.; Bianchi, D.; Chovelon, J.M.; Conchon, P.; Ferronato, C.; Lair, A.; Sleiman, M. Photocatalytic degradation of organic pollutants in water and in air. An analytical approach. *Mater. Sci. Eng. C* **2008**, *28*, 722–725. [CrossRef]
77. Debono, O.; Thevenet, F.; Gravejat, P.; Hequet, V.; Raillard, C.; Lecoq, L.; Locoge, N. Toluene photocatalytic oxidation at ppbv levels: Kinetic investigation and carbon balance determination. *Appl. Catal. B Environ.* **2011**, *106*, 600–608. [CrossRef]

78. Debono, O.; Thévenet, F.; Gravejat, P.; Héquet, V.; Raillard, C.; Le Coq, L.; Locoge, N. Gas phase photocatalytic oxidation of decane at ppb levels: Removal kinetics, reaction intermediates and carbon mass balance. *J. Photochem. Photobiol. A Chem.* **2013**, *258*, 17–29. [CrossRef]
79. Zhong, L.; Haghighat, F.; Lee, C.S.; Lakdawala, N. Performance of ultraviolet photocatalytic oxidation for indoor air applications: Systematic experimental evaluation. *J. Hazard. Mater.* **2013**, *261*, 130–138. [CrossRef] [PubMed]
80. Dong, F.; Wang, Z.; Li, Y.; Ho, W.K.; Lee, S.C. Immobilization of polymeric g-C_3N_4 on structured ceramic foam for efficient visible light photocatalytic air purification with real indoor illumination. *Environ. Sci. Technol.* **2014**, *48*, 10345–10353. [CrossRef]
81. Nuño, M.; Ball, R.J.; Bowen, C.R. Study of solid/gas phase photocatalytic reactions by electron ionization mass spectrometry. *J. Mass Spectrom.* **2014**, *49*, 716–726. [CrossRef]
82. Imoberdorf, G.E.; Cassano, A.E.; Irazoqui, H.A.; Alfano, O.M. Optimal design and modeling of annular photocatalytic wall reactors. *Catal. Today* **2007**, *129*, 118–126. [CrossRef]
83. Imoberdorf, G.E.; Irazoqui, H.A.; Cassano, A.E.; Alfano, O.M. Photocatalytic Degradation of Tetrachloroethylene in Gas Phase on TiO_2 Films: A Kinetic Study. *Ind. Eng. Chem. Res.* **2005**, *44*, 6075–6085. [CrossRef]
84. Héquet, V.; Batault, F.; Raillard, C.; Thévenet, F.; Le Coq, L.; Dumont, É. Determination of the clean air delivery rate (CADR) of photocatalytic oxidation (PCO) purifiers for indoor air pollutants using a closed-loop reactor. Part II: Experimental results. *Molecules* **2017**, *22*, 408. [CrossRef]
85. Xu, T.; Zheng, H.; Zhang, P. Performance of an innovative VUV-PCO purifier with nanoporous TiO_2 film for simultaneous elimination of VOCs and by-product ozone in indoor air. *Build. Environ.* **2018**, *142*, 379–387. [CrossRef]
86. Onoda, K.; Yoshikawa, S. Applications of anodized TiO_2 films for environmental purifications. *Appl. Catal. B Environ.* **2008**, *80*, 277–285. [CrossRef]
87. Taranto, J.; Frochot, D.; Pichat, P. Photocatalytic treatment of air: Comparison of various TiO_2, coating methods, and supports using methanol or n-Octane as tst pollutant. *Ind. Eng. Chem. Res.* **2009**, *48*, 6229–6236. [CrossRef]
88. El-Kalliny, A.S.; Ahmed, S.F.; Rietveld, L.C.; Appel, P.W. Immobilized photocatalyst on stainless steel woven meshes assuring efficient light distribution in a solar reactor. *Drink. Water Eng. Sci.* **2014**, *7*, 41–52. [CrossRef]
89. Monteiro, R.A.R.; Silva, A.M.T.; Ângelo, J.R.M.; Silva, G.V.; Mendes, A.M.; Boaventura, R.A.R.; Vilar, V.J.P. Photocatalytic oxidation of gaseous perchloroethylene over TiO_2 based paint. *J. Photochem. Photobiol. A Chem.* **2015**, *311*, 41–52. [CrossRef]
90. Pulišová, P.; Boháček, J.; Šubrt, J.; Szatmáry, L.; Bezdička, P.; Večerníková, E.; Balek, V. Thermal behaviour of titanium dioxide nanoparticles prepared by precipitation from aqueous solutions. *J. Therm. Anal. Calorim.* **2010**, *101*, 607–613. [CrossRef]
91. Motola, M.; Satrapinskyy, L.; Roch, T.; Šubrt, J.; Kupčík, J.; Klementová, M.; Jakubičková, M.; Peterka, F.; Plesch, G. Anatase TiO_2 nanotube arrays and titania films on titanium mesh for photocatalytic NOX removal and water cleaning. *Catal. Today* **2017**, *287*, 59–64. [CrossRef]
92. Ma, C.M.; Ku, Y.; Kuo, Y.L.; Chou, Y.C.; Jeng, F.T. Effects of silver on the photocatalytic degradation of gaseous Isopropanol. *Water. Air. Soil Pollut.* **2009**, *197*, 313–321. [CrossRef]
93. Xu, W.; Raftery, D. Photocatalytic oxidation of 2-propanol on TiO_2 powder and TiO_2 monolayer catalysts studied by solid-state NMR. *J. Phys. Chem. B* **2001**, *105*, 4343–4349. [CrossRef]
94. Ao, C.H.; Lee, S.C.; Mak, C.L.; Chan, L.Y. Photodegradation of volatile organic compounds (VOCs) and NO for indoor air purification using TiO_2: Promotion versus inhibition effect of NO. *Appl. Catal. B Environ.* **2003**, *42*, 119–129. [CrossRef]
95. Marinangeli, R.E.; Ollis, D.F. Photo-assisted heterogeneous catalysis with optical fibers II. Nonisothermal single fiber and fiber bundle. *AIChE J.* **1980**, *26*, 1000–1008. [CrossRef]
96. Verbruggen, S.W.; Ribbens, S.; Tytgat, T.; Hauchecorne, B.; Smits, M.; Meynen, V.; Cool, P.; Martens, J.A.; Lenaerts, S. The benefit of glass bead supports for efficient gas phase photocatalysis: Case study of a commercial and a synthesised photocatalyst. *Chem. Eng. J.* **2011**, *174*, 318–325. [CrossRef]
97. Hachem, C.; Bocquillon, F.; Zahraa, O.; Bouchy, M. Decolourization of textile industry wastewater by the photocatalytic degradation process. *Dye. Pigment.* **2001**, *49*, 117–125. [CrossRef]

98. Doll, T.E.; Frimmel, F.H. Development of easy and reproducible immobilization techniques using TiO_2 for photocatalytic degradation of aquatic pollutants. *Acta Hydrochim. Hydrobiol.* **2004**, *32*, 201–213. [CrossRef]
99. Herrmann, J.M.; Tahiri, H.; Ait-Ichou, Y.; Lassaletta, G.; González-Elipe, A.R.; Fernandez, A. Characterization and photocatalytic activity in aqueous medium of TiO_2 and Ag-TiO_2 coatings on quartz. *Appl. Catal. B Environ.* **1997**, *13*, 219–228. [CrossRef]
100. Fernández, A.; Lassaletta, G.; Jiménez, V.M.; Justo, A.; González-Elipe, A.R.; Herrmann, J.M.; Tahiri, H.; Ait-Ichou, Y. Preparation and characterization of TiO_2 photocatalysts supported on various rigid supports (glass, quartz and stainless steel). Comparative studies of photocatalytic activity in water purification. *Appl. Catal. B Environ.* **1995**, *7*, 49–63. [CrossRef]
101. Rodgher, V.; Moreira, J.; de Lasa, H.; Serrano, B. Photocatalytic degradation of malic acid using a thin coated TiO_2 -film: Insights on the mechanism of photocatalysis. *AIChE J.* **2014**, *60*, 3286–3299. [CrossRef]
102. Harizanov, O.; Harizanova, A. Development and investigation of sol-gel solutions for the formation of TiO_2 coatings. *Sol. Energy Mater. Sol. Cells* **2000**, *63*, 185–195. [CrossRef]
103. Yamazaki-Nishida, S.; Nagano, K.; Phillips, L.A.; Cervera-March, S.; Anderson, M.A. Photocatalytic degradation of trichloroethylene in the gas phase using titanium dioxide pelle. *J. Photochem. Photobiol. A Chem.* **1993**, *70*, 95–99. [CrossRef]
104. Singh, A.K.; Singh, J.K. Fabrication of durable superhydrophobic coatings on cotton fabrics with photocatalytic activity by fluorine-free chemical modification for dual-functional water purification. *New J. Chem.* **2017**, *41*, 4618–4628. [CrossRef]
105. Langlet, M.; Kim, A.; Audier, M.; Herrmann, J.M. Sol-gel preparation of photocatalytic TiO_2 films on polymer substrates. *J. Sol-Gel Sci. Technol.* **2002**, *25*, 223–234. [CrossRef]
106. Yamazaki, S.; Tanimura, T.; Yoshida, A.; Hori, K. Reaction mechanism of photocatalytic degradation of chlorinated ethylenes on porous TiO_2 pellets: Cl radical-initiated mechanism. *J. Phys. Chem. A* **2004**, *108*, 5183–5188. [CrossRef]
107. Harizanov, O.A.; Gesheva, K.A.; Stefchev, P.L. Sol-gel and CVD-metal oxide coatings for solar energy utilization. *Ceram. Int.* **1996**, *22*, 91–94. [CrossRef]
108. Rachel, A.; Subrahmanyam, M.; Boule, P. Comparison of photocatalytic efficiencies of TiO_2 in suspended and immobilised form for the photocatalytic degradation of nitrobenzenesulfonic acids. *Appl. Catal. B Environ.* **2002**, *37*, 301–308. [CrossRef]
109. Farhanian, D.; Haghighat, F.; Lee, C.S.; Lakdawala, N. Impact of design parameters on the performance of ultraviolet photocatalytic oxidation air cleaner. *Build. Environ.* **2013**, *66*, 148–157. [CrossRef]
110. Zhong, L.; Haghighat, F. Photocatalytic air cleaners and materials technologies—Abilities and limitations. *Build. Environ.* **2015**, *91*, 191–203. [CrossRef]
111. Salaices, M.; Serrano, B.; de Lasa, H.I. Photocatalytic conversion of phenolic compounds in slurry reactors. *Chem. Eng. Sci.* **2004**, *59*, 3–15. [CrossRef]
112. Moreira, J.; Serrano, B.; Ortiz, A.; de Lasa, H. A unified kinetic model for phenol photocatalytic degradation over TiO_2 photocatalysts. *Chem. Eng. Sci.* **2012**, *78*, 186–203. [CrossRef]
113. Legrini, O.; Oliveros, E.; Braun, A.M. Photochemical Processes for Water Treatment. *Chem. Rev.* **1993**, *93*, 671–698. [CrossRef]
114. Ortiz-Gomez, A.; Serrano-Rosales, B.; Salaices, M.; De Lasa, H. Photocatalytic oxidation of phenol: Reaction network, kinetic modeling, and parameter estimation. *Ind. Eng. Chem. Res.* **2007**, *46*, 7394–7409. [CrossRef]
115. Guayaquil, J.F.; Escobedo, S.; Calzada, A.; Serrano, B.; de Lasa, H. Hydrogen Production via Water Dissociation Using Pt–TiO2 Photocatalysts: An Oxidation–Reduction Network. *Catalysts* **2017**, *7*, 324. [CrossRef]
116. Yu, Q.L.; Ballari, M.M.; Brouwers, H.J.H. Indoor air purification using heterogeneous photocatalytic oxidation. Part II: Kinetic study. *Appl. Catal. B Environ.* **2010**, *99*, 58–65. [CrossRef]
117. Besov, A.S.; Vorontsov, A.V.; Parmon, V.N. Fast adsorptive and photocatalytic purification of air from acetone and dimethyl methylphosphonate by TiO_2 aerosol. *Appl. Catal. B Environ.* **2009**, *89*, 602–612. [CrossRef]
118. Boulamanti, A.K.; Philippopoulos, C.J. Photocatalytic degradation of C_5-C_7 alkanes in the gas-phase. *Atmos. Environ.* **2009**, *43*, 3168–3174. [CrossRef]
119. Weibel, A.; Bouchet, R.; Knauth, P. Electrical properties and defect chemistry of anatase (TiO_2). *Solid State Ionics* **2006**, *177*, 229–236. [CrossRef]
120. Sauer, L.M.; Ollis, F.D. Acetone Oxidation in Photocatalytic Monolith Reactor. *J. Catal.* **1994**, *149*, 81–94. [CrossRef]

121. Trong On, D.; Desplantier-Giscard, D.; Danumah, C.; Kaliaguine, S. ChemInform Abstract: Perspectives in Catalytic Applications of Mesostructured Materials. *ChemInform* **2010**, *33*, 299–357. [CrossRef]
122. Maudhuit, A.; Raillard, C.; Héquet, V.; Le Coq, L.; Sablayrolles, J.; Molins, L. Adsorption phenomena in photocatalytic reactions: The case of toluene, acetone and heptane. *Chem. Eng. J.* **2011**, *170*, 464–470. [CrossRef]
123. Obee, T.N. Photooxidation of sub-parts-per-million toluene and formaldehyde levels on titania using a glass-plate reactor. *Environ. Sci. Technol.* **1996**, *30*, 3578–3584. [CrossRef]
124. Ding, X.; An, T.; Li, G.; Zhang, S.; Chen, J.; Yuan, J.; Zhao, H.; Chen, H.; Sheng, G.; Fu, J. Preparation and characterization of hydrophobic TiO_2 pillared clay: The effect of acid hydrolysis catalyst and doped Pt amount on photocatalytic activity. *J. Colloid Interface Sci.* **2008**, *320*, 501–507. [CrossRef]
125. Zhang, Y.P.; Yang, R.; Xu, Q.J.; Mo, J.H. Characteristics of photocatalytic oxidation of toluene, benzene, and their mixture. *J. Air Waste Manag. Assoc.* **2007**, *57*, 94–101. [CrossRef]
126. Chin, P.; Yang, L.P.; Ollis, D.F. Formaldehyde removal from air via a rotating adsorbent combined with a photocatalyst reactor: Kinetic modeling. *J. Catal.* **2006**, *237*, 29–37. [CrossRef]
127. Chen, W.; Zhang, J.S. UV-PCO device for indoor VOCs removal: Investigation on multiple compounds effect. *Build. Environ.* **2008**, *43*, 246–252. [CrossRef]
128. Zhong, L.; Haghighat, F.; Blondeau, P.; Kozinski, J. Modeling and physical interpretation of photocatalytic oxidation efficiency in indoor air applications. *Build. Environ.* **2010**, *45*, 2689–2697. [CrossRef]
129. Salvadores, F.; Alfano, O.M.; Ballari, M.M. Kinetic study of air treatment by photocatalytic paints under indoor radiation source: Influence of ambient conditions and photocatalyst content. *Appl. Catal. B Environ.* **2020**, *268*, 118694. [CrossRef]
130. Yuan, Y.; Zheng, J.; Zhang, X.; Li, Z.; Yu, T.; Ye, J.; Zou, Z. $BaCeO_3$ as a novel photocatalyst with 4f electronic configuration for water splitting. *Solid State Ionics* **2008**, *178*, 1711–1713. [CrossRef]
131. Jacoby, W.A.; Blake, D.M.; Noble, R.D.; Koval, C.A. Kinetics of theoxidation of trichloroethylene in air via heterogeneous photocatalysis. *J. Catal.* **1995**, *157*, 87–96. [CrossRef]
132. Baxter, R.J.; Hu, P. Insight into why the Langmuir-Hinshelwood mechanism is generally preferred. *J. Chem. Phys.* **2002**, *116*, 4379–4381. [CrossRef]
133. Vincent, G.; Marquaire, P.M.; Zahraa, O. Photocatalytic degradation of gaseous 1-propanol using an annular reactor: Kinetic modelling and pathways. *J. Hazard. Mater.* **2009**, *161*, 1173–1181. [CrossRef]
134. Zhong, L.; Haghighat, F. Modeling and validation of a photocatalytic oxidation reactor for indoor environment applications. *Chem. Eng. Sci.* **2011**, *66*, 5945–5954. [CrossRef]
135. Lopes, F.V.S.; Monteiro, R.A.R.; Silva, A.M.T.; Silva, G.V.; Faria, J.L.; Mendes, A.M.; Vilar, V.J.P.; Boaventura, R.A.R. Insights into UV-TiO_2 photocatalytic degradation of PCE for air decontamination systems. *Chem. Eng. J.* **2012**, *204–205*, 244–257. [CrossRef]
136. Vorontsov, A.V.; Stoyanova, I.V.; Kozlov, D.V.; Simagina, V.I.; Savinov, E.N. Kinetics of the photocatalytic oxidation of gaseous acetone over platinized titanium dioxide. *J. Catal.* **2000**, *189*, 360–369. [CrossRef]
137. Valadés-Pelayo, P.J.; Guayaquil Sosa, F.; Serrano, B.; de Lasa, H. Eight-lamp externally irradiated bench-scale photocatalytic reactor: Scale-up and performance prediction. *Chem. Eng. J.* **2015**, *282*, 142–151. [CrossRef]
138. Fuller, E.N.; Schettler, P.D.; Giddings, J.C. A new method for prediction of binary gas-phase diffusion coefficients. *Ind. Eng. Chem.* **1966**, *58*, 18–27. [CrossRef]
139. Degrave, R.; Moreau, J.; Cockx, A.; Schmitz, P. Multiscale analysis and modelling of fluid flow within a photocatalytic textile. *Chem. Eng. Sci.* **2015**, *130*, 264–274. [CrossRef]
140. Cassano, A.E.; Martín, C.A.; Brandi, R.J.; Alfano, O.M. Photoreactor Analysis and Design: Fundamentals and Applications. *Ind. Eng. Chem. Res.* **1995**, *34*, 2155–2201. [CrossRef]
141. Davydov, L.; Smirniotis, P.G.; Pratsinis, S.E. Novel differential reactor for the measurement of overall quantum yields. *Ind. Eng. Chem. Res.* **1999**, *38*, 1376–1383. [CrossRef]
142. Valadés-Pelayo, P.J.; Moreira del Rio, J.; Solano-Flores, P.; Serrano, B.; de Lasa, H. Establishing photon absorption fields in a Photo-CREC Water II Reactor using a CREC-spectroradiometric probe. *Chem. Eng. Sci.* **2014**, *116*, 406–417. [CrossRef]
143. Serrano, B.; De Lasa, H. Photocatalytic Degradation of Water Organic Pollutants. Kinetic Modeling and Energy Efficiency. *Ind. Eng. Chem. Res.* **1997**, *36*, 4705–4711. [CrossRef]

144. Tran Thi Thuong, H.; Tran Thi Kim, C.; Nguyen Quang, L.; Kosslick, H. Highly active brookite TiO_2-assisted photocatalytic degradation of dyes under the simulated solar−UVA radiation. *Prog. Nat. Sci. Mater. Int.* **2019**, *29*, 641–647. [CrossRef]
145. Di Paola, A.; Addamo, M.; Bellardita, M.; Cazzanelli, E.; Palmisano, L. Preparation of photocatalytic brookite thin films. *Thin Solid Films* **2007**, *515*, 3527–3529. [CrossRef]
146. Jin, J.; Chen, S.; Wang, J.; Chen, C.; Peng, T. $SrCO_3$ -modified brookite/anatase TiO_2 heterophase junctions with enhanced activity and selectivity of CO2 photoreduction to CH4. *Appl. Surf. Sci.* **2019**, *476*, 937–947. [CrossRef]
147. Cao, S.; Chan, T.S.; Lu, Y.R.; Shi, X.; Fu, B.; Wu, Z.; Li, H.; Liu, K.; Alzuabi, S.; Cheng, P.; et al. Photocatalytic pure water splitting with high efficiency and value by Pt/porous brookite TiO_2 nanoflutes. *Nano Energy* **2020**, *67*, 104287. [CrossRef]
148. Wang, H.; Gao, X.; Duan, G.; Yang, X.; Liu, X. Facile preparation of anatase-brookite-rutile mixed-phase N-doped TiO_2 with high visible-light photocatalytic activity. *J. Environ. Chem. Eng.* **2015**, *3*, 603–608. [CrossRef]
149. Ma, Y.; Kobayashi, K.; Cao, Y.; Ohno, T. Development of visible-light-responsive morphology-controlled brookite TiO_2 nanorods by site-selective loading of AuAg bimetallic nanoparticles. *Appl. Catal. B Environ.* **2019**, *245*, 681–690. [CrossRef]
150. Svobodova, A.; Walterova, D.; Vostalova, J. Ultraviolet light induced alteration to the skin. *Biomed. Pap. Med. Fac. Univ. Palacky. Olomouc. Czech. Repub.* **2006**, *150*, 25–38. [CrossRef] [PubMed]
151. Gonzaga, E.R. Role of UV Light in Photodamage, Skin Aging, and Skin Cancer. *Am. J. Clin. Dermatol.* **2009**, *10*, 19–24. [CrossRef]
152. Young, A.R. Acute effects of UVR on human eyes and skin. *Prog. Biophys. Mol. Biol.* **2006**, *92*, 80–85. [CrossRef]
153. Paz, Y. Application of TiO_2 photocatalysis for air treatment: Patents' overview. *Appl. Catal. B Environ.* **2010**, *99*, 448–460. [CrossRef]
154. Goswami, D.Y. Decontamination of ventilation systems using photocatalytic air cleaning technology. *J. Sol. Energy Eng. Trans. ASME* **2003**, *125*, 359–365. [CrossRef]
155. Chotigawin, R.; Sribenjalux, P.; Supothina, S.; Johns, J.; Charerntanyarak, L.; Chuaybamroong, P. Airborne Microorganism Disinfection by Photocatalytic HEPA Filter. *EnvironmentAsia* **2010**, *3*, 1–7.
156. Pigeot-Remy, S.; Lazzaroni, J.C.; Simonet, F.; Petinga, P.; Vallet, C.; Petit, P.; Vialle, P.J.; Guillard, C. Survival of bioaerosols in HVAC system photocatalytic filters. *Appl. Catal. B Environ.* **2014**, *144*, 654–664. [CrossRef]
157. Stuart, J.I.; Salaices, M.; Valvano, M.A.; De Lasa, H.I. Photocatalytic Inactivation of MS2 Bacteriophage and *E. coli.* Kinetics Modeling and Quantum Efficiency. In Proceedings of the 18th North American Catalysis Society Conference, Cancun, Mexico, 1–6 June 2003; pp. 1–2. Available online: http://nacatsoc.org/18nam/Orals/257-PhotocatalyticInactivationofMS2Bacteriophage.pdf (accessed on 20 April 2020).
158. Armon, R.; Narkis, N.; Neeman, I. Photocatalytic Inactivation of Different Bacteria and Bacteriophages in Drinking Water at Different TiO_2 Concentration With or Without Exposure to O_2. *J. Adv. Oxid. Technol.* **1998**, *3*. [CrossRef]